Available online at www.sciencedirect.com

ScienceDirect

Geochimica et Cosmochimica Acta 284 (2020) 173–195

Geochimica et Cosmochimica Acta

www.elsevier.com/locate/gca

Evidence for diverse lunar melt compositions and mixing of the pre-3.9 Ga crust from zircon chemistry

Dustin Trail [a,*], Mélanie Barboni [b], Kevin D. McKeegan [c]

[a] Department of Earth & Environmental Sciences, University of Rochester, Rochester, NY 14627, USA
[b] School of Earth and Space Exploration, Arizona State University, Tempe, AZ 85287, USA
[c] Department of Earth, Planetary, and Space Sciences, University of California – Los Angeles, Los Angeles, CA 90095, USA

Received 19 February 2020; accepted in revised form 18 June 2020; available online 27 June 2020

Abstract

Lunar samples collected during Apollo missions are typically impact-related breccias or regolith that contain amalgamations of rocks and minerals with various origins (e.g., products of igneous differentiation, mantle melting, and/or impact events). The largest intact pre-Nectarian (~≥3.92 Ga) fragments of igneous rock contained within the breccia and regolith rarely exceed 1 cm in size, and they often show evidence for impact recrystallization. This widespread mixing of disparate materials makes unraveling the magmatic history of pre-Nectarian period fraught with challenges. To address this issue, we combine U-Pb geochronology of Apollo 14 zircons (^{207}Pb–^{206}Pb ages from 3.93 to 4.36 Ga) with zircon trace element chemistry and thermodynamic models. Zircon crystallization temperatures are calculated with Ti-in-zircon thermometry after presenting new titania and silica activity models for lunar melts. We also present rare earth element (REE), P, actinide, and Mg + Fe + Al concentrations. While REE patterns and P yield little information about the parent melt origins of these out-of-context grains, U and Th concentrations are highly variable among pre-4.2 Ga zircons when compared to younger grains. Thus, the distribution of heat-producing radioactive elements in melt sources pervading the early lunar crust was heterogenous. Melt composition variation is confirmed by zircon Al concentrations and thermodynamic modeling that reveal at least two dominant magma signatures in the pre-4.0 Ga zircon population. One inferred magma type has a high alumina activity. This magma likely assimilated anorthosite-rich rocks (e.g., Feldspathic Highlands Terrane; FHT), though impact-generated melts of an alumina-rich target rock is a viable alternative. The other magma signature bears more similarities to KREEP basalts from the Procellarum KREEP Terrane (PKT), reflecting lower apparent alumina activities. Melt diversity seems to disappear after 4.0 Ga, with zircon recording magma compositions that largely fall in-between the two main groups found for pre-4.0 Ga samples. We interpret <4 Ga zircons to have formed from a mixture of KREEP basalts and FHT-like rocks, consistent with the upper ~15 km of the crust being thoroughly mixed and re-melted by basin-forming impacts during the pre-Nectarian period.

Keywords: Apollo; Lunar; Zircon; KREEP; Thorium; Ti-in-zircon; Imbrium; Anorthosite; Impact

1. INTRODUCTION

Before the Apollo missions, some thought that the Moon was a primitive, undifferentiated body, that could have been the source of some chondritic meteorites (e.g. Urey, 1966). However, petrological and geochemical investigations of Apollo samples revealed a differentiated,

* Corresponding author.
E-mail address: dtrail@ur.rochester.edu (D. Trail).

https://doi.org/10.1016/j.gca.2020.06.018
0016-7037/

geologically complex body. One of the lasting models developed through investigations of these samples was the concept of a global lunar magma ocean (LMO) (e.g., Wood et al., 1970; Warren, 1985). This model, which is based on the hypothesis that the early Moon solidified fractionally from a totally or near totally-molten body, explains mineralogical observations such as the dominant lunar highland ferroan anorthosite (FAN) flotation crust (Feldspathic Highlands Terrane; FHT), an ultramafic mantle rich in olivine and pyroxene, and the cumulate textures of anorthositic clasts from Apollo breccias, requiring extensive melting and crystal fractionation (Jolliff et al., 2000). The LMO culminated with a potassium (K) + rare-earth element (REE) + phosphorus (P)-rich residual (i.e., KREEP component) after significant fractional crystallization. The KREEP reservoir is believed to be largely concentrated in the Procellarum KREEP Terrane (PKT) (Jolliff et al., 2000; Laneuville et al., 2013), though its presence is inferred in the highlands terrane based on heterogenous REE and actinide contents in FAN clasts (e.g., Pernet-Fischer et al., 2019). Such igneous samples, along with the production of Mg- and alkali-suite rocks, largely reflect endogenous (internal) lunar magmatism that can help decipher the planetary evolution occurring after main-stage accretion.

The lunar surface has, however, been significantly altered by a complex history of impacts that have obscured the nature of early magmatism. While the flux and frequency of this history is debated, lunar rocks remain our best record of the early impact history of the inner solar system (e.g. Tera et al. 1974; Hartmann, 1975; Cohen et al., 2000; Ryder et al., 2000; Boehnke and Harrison, 2016; Zellner, 2017). In this context, lunar petrology, geochemistry, and chronology are closely studied by the dynamical community to inform their models. Numerical simulations are updated to reflect the state-of-the-art geochemical studies to explain the source of the impactors, thermal consequences for the crust of the terrestrial bodies, and the dynamics of the entire solar system (Gomes et al., 2005; Strom et al., 2005; Morbidelli et al., 2012; Genda et al., 2017). These studies also have direct relevance to the early terrestrial environment including an emergent biosphere (Chyba et al., 1990; Abramov and Mojzsis, 2009; Brasser et al., 2016).

For these reasons, it is important to accurately decipher the early magmatic history (i.e., the first ~600 Ma) of the Moon. This is not straight forward, because lunar rocks record a mixture of endogenous and exogenous processes, imperfectly preserving chemical signatures inherited from early magmatism which are potentially overprinted by secondary impact heating. If a rock fragment (or mineral) is endogenously generated, this chemical information is directly relevant to planetary formation, differentiation, and subsequent magmatism. If exogenous, the chemistry is more relevant to discovering how impacts can alter the chemical evolution of planetary bodies. Distinguishing between these possibilities is a challenge that is compounded by sample availability. It is estimated, for example, that of the ~400 kg of material returned by the Apollo missions, less than 1% represent coherent fragments of pre-Nectarian (~≥3.92 Ga) lithologies (Taylor et al., 1983; Shearer et al., 2006a; Wieczorek et al., 2006).

The complexities due to pervasive brecciation of lunar rocks that compromise interpretation of early lunar history can be ameliorated to some extent through analysis of single grains of the chemically and physically robust mineral zircon ($ZrSiO_4$). Zircons form in differentiated felsic melts during endogenous and exogenous processes on the Moon, and they can retain age information as well as chemical and isotopic signatures for billions of years (e.g., Cherniak and Watson, 2000). Several studies have reported U-Pb ages of more than 400 zircons from the Apollo collection, with ^{207}Pb-^{206}Pb ages from ~4.4 to 3.9 Ga (Meyer et al., 1996; Nemchin et al., 2006, 2008; Pidgeon et al., 2007; Taylor et al., 2009; Grange et al., 2009, 2011, 2013a,b; Hopkins and Mojzsis, 2015; Crow et al., 2017; Barboni et al., 2017). Some zircons have morphologies and/or crystal structures indicative of formation (or recrystallization) during impact events (e.g., Grange et al., 2013a,b; Crow et al., 2017). Others are found in small clasts assumed to represent their parent lithology (e.g., Meyer et al., 1996; Nemchin et al., 2012). However, the vast majority of lunar zircons thus far investigated are derived from breccias (or soils) and do not have morphologies or petrographic context that provide direct information about their origins. They may have been formed during impact melting, or some other primary process with physical and chemical characteristics consistent with igneous crystallization, possibly from a KREEP-like source (e.g., Taylor et al., 2009). It is also possible that those zircons contained within a lithic clast may be inherited; that is, they may have actually formed in a different lithology.

To better understand the origins of these grains and what they can tell us about the evolutionary history of the lunar crust, we need new chemical tools capable of revealing the petrogenesis of out-of-context zircon. Here, we couple Al contents in zircon (X_{Al}^{Zrc}) with detailed thermodynamic modeling to infer zircon parent melt properties. We complement this new information with U-Th-Pb geochronology, Ti-in-zircon thermometry, new models for silica and titania activities of lunar melts, and zircon rare earth element (REE) plus Fe + Mg concentrations. We find evidence for two major and at least one minor pre-4.0 Ga melt composition from analysis of Apollo 14 zircon chemistry. Evidence is based primarily on X_{Al}^{Zrc} coupled with a thermodynamic model. We also find evidence for heterogenous U and Th contents in pre-4.2 Ga melts. The chemical tracers applied here provide consistent lines of evidence that zircon parent melts were more homogenous after 4.2 Ga. It is even possible that two of the pre-4.2 Ga rock types may have been mixed and re-melted to form <4 Ga grains.

2. SAMPLES

Four different samples from Apollo 14 were processed for zircon following previous procedures (e.g., Taylor et al., 2009; Crow et al., 2017). The sample preparation methods can be found in Electronic Annex 1 (EA-1). The majority of zircons are from Apollo sample 14311, 58. The 14311 parent rock is a polymict impact melt breccia and is among the largest samples collected from Apollo 14 (Simonds et al. 1977). In many respects this sample is

ideal because previous studies have identified a 500 Myr range with at least three populations identified in zircon ages (e.g., Meyer et al., 1989; Meyer et al., 1996; Hopkins and Mojzsis, 2015; Merle et al., 2017); thus, we expect the zircons in this breccia to sample a diverse range of lunar lithologies. Apollo 14 soil samples 14163 and 14259 were chosen due to the presence of previously documented felsic components in the glass (Aitken et al., 1971; Labotka et al., 1980; Papike et al. 1982). Because zircon is more common in differentiated felsic rocks, the likelihood of finding zircon in these soil samples is presumed to be higher. We provide a summary of sample numbers, sample types, zircon yields, and the number of zircons measured by each analytical method in Table 1.

3. ANALYTICAL METHODS

3.1. U-Th-Pb geochronology

U-Th-Pb dating was performed on the UCLA CAMECA *ims*1290 using the Hyperion-II ion source for the primary beam. The Hyperion-II produces an oxygen ion beam with very low energy dispersion, leading to significantly higher beam brightness and thus smaller diameter beam spots (for a given current) compared to the duoplasmatron ion source (Liu et al., 2018). Samples were Au sputter coated prior to analysis with a primary current of ~10 nA, corresponding to a spot size of *ca.* 4 μm – see Electronic Annex EA-1. Our operating conditions were otherwise similar to the established ion microprobe U-Pb procedures, as described in Quidelleur et al. (1997). We used a MRP (mass resolving power) of about 6000 with a 50 eV energy window and a 15 eV offset for $^{238}U^{+}$. To compensate for the contrasting energy distribution of $^{206}Pb^{+}$ and $^{254}UO^{+}$ with respect to $^{238}U^{+}$, we applied a relative sensitive factor (RSF) based upon 92 analyses of zircon standard AS3 (1099 ± 0.5 Ma; Paces and Miller, 1993). The variability of $^{254}UO^{+}/^{238}U^{+}$ vs. $^{206}Pb/^{238}U^{+}$ calibration for AS-3 zircon used to correct our U-Pb lunar zircon data can be found in EA-1.

Because Apollo zircons have low U contents, average precision on $^{206}Pb/^{238}U$ ages is ca. 2%, limited primarily by counting statistics for single spot analyses. This precision was considered acceptable for purposes of this study and therefore U-Pb ages were typically obtained for only one spot on each zircon, to conserve sample surface area for other trace element analyses. The most likely source of common Pb contamination was from sample preparation; therefore, all data were reduced with a common Pb composition of California surface waters reported by Sañudo-Wilhelmy and Flegal (1994), although in practice the exact isotopic composition is of minor importance since all samples showed radiogenic $^{206}Pb^{*}$ contents >99.7% (see EA-2). We targeted clean regions of grains with apparently simple features. We note that there are rare cases among the zircons studied here that have textural characteristics indicative of impact disruption (e.g., see CL image 14311_27 in EA-1), but these grain regions were not targeted for study.

3.2. Al and Ti in zircon measurements

Lunar zircon Al and Ti contents were also measured with the UCLA CAMECA *ims*1290. Epoxy mounts were ultrasonically cleaned in a sequence of soapy water, deionized water, and methanol, and then carbon coated. While Au coating is possible, the ring holder for the Au source in the sputter coater is made of Al and might therefore be a source of contamination thus requiring more intensive ion cleaning of the surface for robust measurements. The samples were analyzed with the Hyperion-II $^{16}O^{-}$ beam (Liu et al., 2018). A primary beam intensity of ~3 nA with a spot size of ~5 μm was used in each analysis. Samples were pre-sputtered for 3 min, followed by ~10 min for data acquisition. Magnetic field peak switching was used to acquire data on the axial ETP electron multiplier for $^{23}Na^{+}$ (2 sec), $^{24}Mg^{+}$ (5 sec), $^{39}K^{+}$ (2 sec), $^{27}Al^{+}$ (10 sec), $^{49}Ti^{+}$ (10 sec), and $^{56}Fe^{+}$ (3 sec) at a MRP of ~4000, which is sufficient to resolve all relevant molecular interferences. In addition, $^{28}Si^{+}$ (2 sec) was measured with a Faraday cup (FC2) and yielded ~2.4×10^{7} cps at ~3 nA. Each acquisition contained 10 cycles.

Zircon Al concentrations (X_{Al}^{Zrc}) were calculated relative to synthetic zircon standards (EA-1). The detailed characteristics of these standards, including the techniques for synthesis, are reported elsewhere (Trail et al., 2011a; Trail et al., 2017; Wang and Trail, 2019). Several evaluations were made to test homogeneity of the candidate synthetic zircon standards before a detailed investigation of lunar zircons was undertaken. The zircon standard produced following the technique of Trail et al. (2011a) was found to be the most homogenous when interrogated with the small size of the Hyperion-II source and it was therefore used as a primary standard for the data reported here.

The major elements Na and K were used primarily as proxies for inclusions or secondary surface contamination. The block data of all samples were carefully monitored for changes in Al/Si etc. as a function of depth before considering the data further. Surface contamination was also a concern. Past analyses of natural samples and experimental studies have revealed that most terrestrial zircons from met-

Table 1
Zircon yields and analyses for Apollo 14 soil and breccia samples.

Sample, sub-sample	Sample type	Zircon yield	U-Th-Pb geochron.	Ti, Al	REE, P, Mg, Fe, Th, U
14311, 58	impact breccia	81	76	70	64
14259, 64	soil sample	3	2	0	3
14259, 511	soil sample	7	5	1	4
14163, 65	soil sample	7	6	6	6
14163, 949	soil sample	4	4	3	3

aluminous rocks which crystallized <800 °C yield X_{Al}^{Zrc} on the order of a few ppm (Trail et al., 2017). With this in mind, we also monitored low X_{Al}^{Zrc} for terrestrial samples. Carefully selected grain regions of Duluth Gabbro AS-3 U-Pb zircon standard, located on the same epoxy mount as lunar zircons, were measured. The average X_{Al}^{Zrc} for AS-3 zircons was ~0.3 ppm, below the Al contents reported for lunar samples (EA-1). The zircon Ti concentrations were determined by standardizing against 91500 (Wiedenbeck et al., 2004), using a recommended concentration of 4.73 ppm (Szymanowskia et al., 2018).

3.3. Rare Earth elements (REEs) and other trace elements

Trace elements, including Mg, P, Fe, Y, REEs, Hf, Th, and U, were measured on the UCLA CAMECA *ims1270* using a ca. 15 nA O^- primary beam focused to a *ca.* 20 μm spot following the procedure of Bell et al. (2016). In some cases, grain regions free of cracks etc. were too small, and so those grains were not analyzed. Data were collected with a 100 eV energy offset to suppress molecular interferences. Relative sensitivity factors were determined using NIST 610 glass with additional comparison to the 91500 standard (e.g., Wiedenbeck et al., 2004). Further details on the method can be found in Schmitt and Vazquez (2006).

4. RESULTS

Ion microprobe data, including U-Pb geochronology and trace element data, can be found in EA-2. Representative zircon images are provided in Fig. 1, and additional images are presented in EA-1. The first row (Fig. 1a–c)

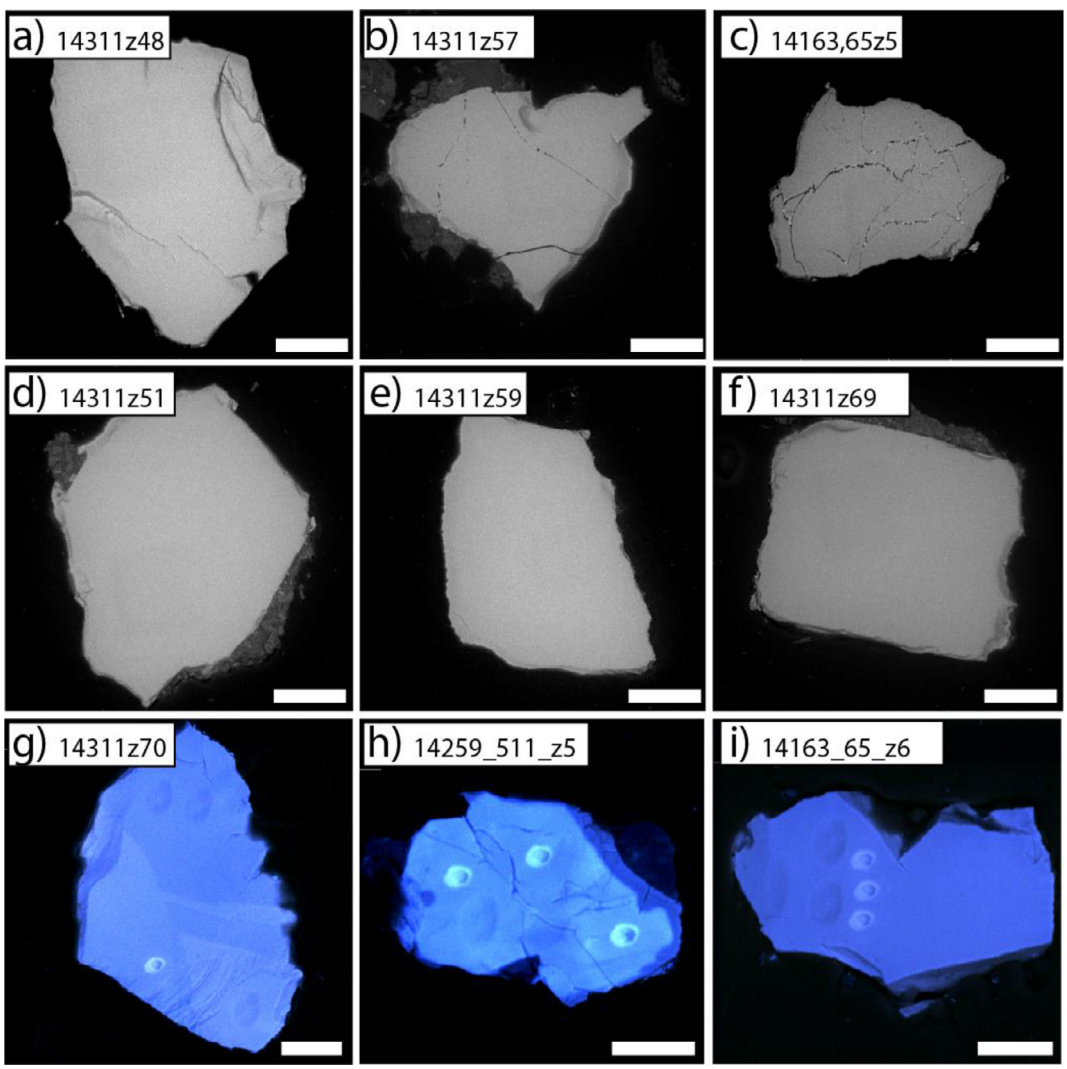

Fig. 1. Backscattered electron (BSE) and cathodoluminescence (CL) images showing typical surface features of zircons analyzed in this study. All scale bars are 50 μm. (a–c) Some grains (images in BSE) contain abundant cracks – identifying grain regions to avoid during analysis – whereas other grains are relatively free of surface features and imperfections (e.g., e–f). (g–i) Example CL images collected after analyses. Hyperion-II spots (*ims*1290 instrument) are represented by the brighter smaller spots; the larger spots were produced by the duoplasmatron (*ims*1270 instrument).

shows grains with abundant cracks and imperfections on the surface – a common occurrence – that were avoided during analysis. Many zircons show regions free of cracks and obvious inclusions (Fig. 1d–f). The cathodoluminescence (CL) images show that many zircons are fragmented, possibly due to fracturing from impacts. In some cases, zoning was observed in CL (Fig. 1g–i).

4.1. U-Pb geochronology

All U-Pb ages are within 5% of concordia except for two grains that exhibit unusual characteristics (EA-2). The two exceptional grains are 14311,58_z15, apparently reversely discordant by 7%, and 14259,511_z5, reversely discordant by 12%. Grain 14311,58_z15 has large ^{207}Pb-^{206}Pb age uncertainties (4205 ± 157 Ma, 1σ). Moreover, it has a ~9% uncertainty in its discordance, which means that it is not 7% reversely discordant once errors are considered (EA-2). The large errors for this grain are because it has the lowest U concentration in the sample suite (~19 ppm). Because of the high error associated with this grain, it is not considered further. In contrast, the other grain (14259,511_z5) that appears to be reversely discordant has the highest U content measured (1500 ppm) of all grains investigated, which is about a factor of 30–50 more than typical lunar zircons and about three times more U than the U-Pb AS-3 standard. This potentially gives rise to a matrix effect in the U/Pb RSF calibration resulting in its apparent reverse discordance. While U-Pb ages may be sufficiently inaccurate due to analytical (matrix) effects, it appears that the ^{207}Pb-^{206}Pb date is well constrained (4225 ± 4 Ma, 1 σ), and we thus consider this grain in our discussions of trace element chemistry correlations with zircon age.

Most new U-Pb zircon geochronology are from sample 14311, which is compared directly to studies that also reported zircon ages for this parent sample (Fig. 2a, Hopkins and Mojzsis, 2015; Merle et al., 2017). We also compare all ^{207}Pb-^{206}Pb ages to other Apollo 14 zircon ages previously reported (Nemchin et al., 2006, 2008; Taylor et al., 2009; Grange et al., 2013; Hopkins and Mojzsis, 2015; Crow et al., 2017; Merle et al. 2017) in Fig. 2b. All studies show a similar age range – from *ca.* 3.93 to 4.4 Ga – but the mode is distinctly different. Our 14311 breccia split contained a much higher occurrence of <4.0 Ga zircons. For comparison, ~35% of the analyzed grain fragments reported here are <4.0 Ga, whereas for all the other studies noted above, the yield of <4.0 Ga zircons is only ~5%. Other age peaks at *ca.* 4.25 and 4.33 Ga, as determined from other studies, were also identified here.

4.2. Zircon Ti concentrations and lunar titania/silica activities for Ti-in-zircon thermometry

The Ti data were carefully examined for contamination prior to thermometry calculations, mindful of observations made by previous workers (Ferry and Watson, 2007). For instance, it has become common practice to monitor the Fe/Ti ratio for each analysis, before reporting Ti contents as robust values associated with the zircon structure (e.g., Hopkins and Mojzsis, 2015; Crow et al., 2017). Crow et al. (2017) chose an apparent Fe content of 400 ppm as a cutoff, based on anticipated maximum Fe contents in zircon (Wopenka et al., 1996), and other statistical analysis of contamination based on terrestrial zircon (Bell et al., 2015). Hopkins and Mojzsis (2015) put a hard line at apparent temperatures greater than >1200 °C (>280 ppm Ti) and rejected these data as part of their contamination filtering procedure. We have also carefully monitored proxies for contamination here as well, and two grains were excluded from further consideration due to contamination. The rejected grains contain average Na^+ counts more than three times greater than for other lunar zircons, and large variability in the ion microprobe block-to-block Al/Si data (EA-1). Zircon Ti concentrations quantified here are broadly comparable with past studies (Fig. 3).

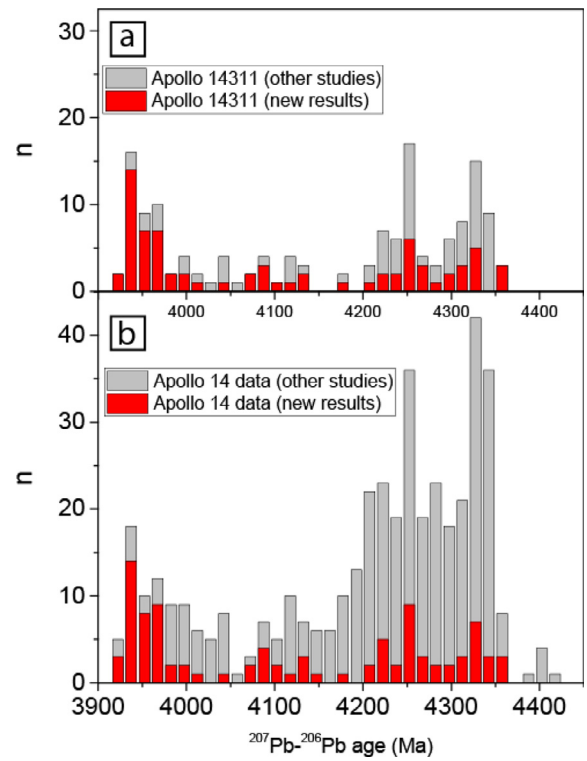

Fig. 2. Age histograms for Apollo 14 grains. Data included from literature sources are not plotted if they are ≥10% discordant. If literature-sourced data contains multiple analyses per zircon, the oldest (<10% discordant) ^{207}Pb-^{206}Pb age is used. The bin size is 15 Ma, commensurate with the average 1 s.d. of ^{207}Pb-^{206}Pb ages reported for all samples (16 Ma). The age range for this study and previously reported results are similar. However, the mode is different: <4 Ga grains comprise about 1/3 of the new results reported here, vs. ~5% from previous studies. (a) Histogram showing only 14311 data for our new results and other 14311 studies (Hopkins and Mojzsis, 2015; Merle et al., 2017), which have age peaks at *ca.* 4.33, 4.24, and 3.94 Ga (n = 148). (b) Plot showing all Apollo 14 data for our new results and literature sources (Nemchin et al., 2006, 2008; Taylor et al., 2009; Grange et al., 2013; Hopkins and Mojzsis, 2015; Merle et al. 2017; Crow et al., 2017) (n = 423).

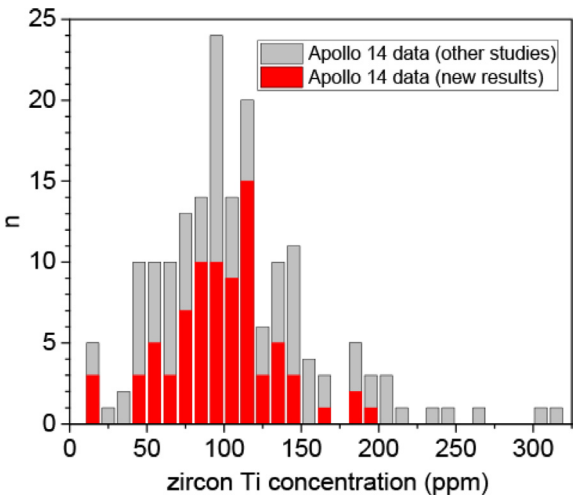

Fig. 3. Zircon Ti concentrations for Apollo 14 samples interpreted to represent clean analyses which also yield U-Pb ages less than 10% discordant (n = 90; Taylor et al., 2009; Hopkins and Mojzsis 2015; Crow et al., 2017; Bellucci et al., 2019). These data compare well to the 80 grains reported here. The main exception being that 9 zircons from former studies yield zircon Ti contents in excess of 200 ppm.

These data were collected to calculate the zircon crystallization temperature through application of the Ti-in-zircon thermometer (e.g., Watson and Harrison, 2005). This calculation requires knowledge of the titania and silica activity of the crystallization environment (Ferry and Watson 2007), which presents a problem because zircons studied here are from polymict breccias or soils with restricted petrological context. To address this, we first constrain the titania activity of the crystallization environment (a_{TiO2}; standard state relative to rutile saturation).

Rutile has in fact been identified in lunar samples (e.g., Hlava et al., 1972; Haggerty, 1973), and it is likely formed from the breakdown of ilmenite by the *subsolidus* reaction:

$$2FeTiO_3(ilmenite) = 2Fe(metal) + 2TiO_2(rutile) + O_2 \quad (1)$$

(Taylor et al., 1972). While it would be appropriate to assume that a_{TiO2} was buffered at ~1 for metamorphic zircon forming with rutile present, most zircons are generally considered to be derived from igneous melts (e.g., Taylor et al., 2009), so this a_{TiO2} constraint not reasonable for most lunar zircons. Other a_{TiO2} constraints have been derived for terrestrial igneous systems. Ghiorso and Gualda (2013) developed a thermodynamic expression to calculate the titania activity of the liquid based upon the spinel (ulvöspinel-magnetite solid solution) and rhombohedral (ilmenite-hematite solid solution) oxide compositions. However, this is probably not useful for the Moon because ulvöspinel tends to break down along the liquid line of descent during cooling via the following (idealized) reaction: $Fe_2TiO_4 = FeTiO_3 + Fe + ½O_2$ (e.g., El Goresy et al., 1971). Thus, the spinel-rhombohedral pair do not crystallize contemporaneously on the Moon (Taylor et al., 1973), and therefore the a_{TiO2} formulation developed by Ghiorso and Gualda, (2013) cannot be applied here.

However, a modified version of Eq. (1) is useful for titania activity constraints:

$$2FeTiO_3(ilmenite) = 2Fe(metal) + 2TiO_2(melt) + O_2 \quad (2)$$

where a_{TiO2}^{melt} is the titania activity in the melt expressed relative to rutile saturation. To calculate a_{TiO2}^{melt} from Eq. (2), ilmenite and Fe-metal need to be present in zircon-saturated melts. There is good reason to think this is the case for ilmenite because titaniferous phases are predicted to saturate well before zircon along the liquid line of descent in mafic (Dickinson and Hess, 1982; Ryerson and Watson, 1987) and felsic ($\pm H_2O$) systems (Dickinson and Hess, 1982; Hayden and Watson, 2007; Boehnke et al., 2013). If Fe-metal is also present (e.g., Sato et al., 1973), the equilibrium constant (K_{IFe}) of Eq. (2) becomes:

$$K_{IFe} = \frac{\left[a_{Fe}^{Fe-metal}\right]^2 \times \left[a_{TiO2}^{melt}\right]^2 \times fO_2}{\left[a_{FeTiO3}^{ilmenite}\right]^2} \quad (3)$$

where $a_{Fe}^{Fe-metal}$ is the activity of Fe in Fe-metal, fO_2 is the oxygen fugacity, and $a_{FeTiO3}^{ilmenite}$ is the activity of $FeTiO_3$ in ilmenite. The titania activity term (a_{TiO2}^{melt}) can be directly calculated if $a_{FeTiO3}^{ilmenite}$, $a_{Fe}^{Fe-metal}$, fO_2, and K_{IFe} are known, which are addressed individually in the next three paragraphs.

Impurities in lunar Fe-metal, which lower $a_{Fe}^{Fe-metal}$, are common in fairly low concentrations. For instance, Fe-metal from Apollo 14 breccia contain average 5–7 at% of Ni and Co total, though rare occurrences up to ~30 at% have been documented (e.g., Gancarz et al., 1971; El Goresy et al., 1971; Taylor et al., 1983). We assume that this level of impurity will have a negligible effect, and therefore $a_{Fe}^{Fe-metal} \approx 1$. While we consider the presence of Fe-metal to be a reasonable assumption, if it is incidentally absent in the zircon crystallization environment, it might cause a_{TiO2}^{melt} to be overestimated. If a_{TiO2}^{melt} is overestimated, the calculated Ti-in-zircon crystallization temperature will be lower than the true value (if all other variables are held equal).

Lunar ilmenite from Apollo 14 and 15 basalts also contain impurities. Ilmenite contains Mg – due to the solid solution between ilmenite ($FeTiO_3$) and geikielite ($MgTiO_3$) – and minor amounts of Cr, Mn, Al, and V, and Zr (El Goresy et al., 1971; Gancarz et al., 1971; Hlava et al., 1972; Taylor et al., 1973; Taylor et al., 1983). In these studies, total impurities make up about ~5 at% of the cations in ilmenite. We assume that the level of impurities are too low to modify the $a_{FeTiO3}^{ilmenite}$ relationships substantially (i.e., $a_{FeTiO3}^{ilmenite} \approx 1$). Moreover, because Fe-metal and ilmenite are on opposite sides of the equilibrium reaction (Eqs. (2) and (3)), sub-unity activity values would tend to compensate for each other.

An fO_2 constraint is also required. Several methods have been used to constrain the fO_2 of lunar melts to the solidus, and values range from the iron-wüstite (IW) equilibrium reaction to 2 log units below IW (Haggerty and Meyer 1970; Nash and Hausel 1973; Sato et al., 1973; Karner et al., 2006). The most recent estimates have converged upon the intermediate values of this range, and we therefore adopt a value of IW-1 here (Wadhwa, 2008; Papike et al., 2016). And finally, the equilibrium constant (K_{IFe}) for

Eq. (3) is required, which was characterized by O'Neill et al. (1988) in the presence of rutile. O'Neill et al. (1988) determined the oxygen potential of the ilmenite-rutile-Fe (metal) equilibria at 1 atm from 990 to 1320 K. Here, we use this equilibrium reaction to solve for a_{TiO2}^{melt} (expressed relative to rutile saturation) with $a_{FeTiO3}^{ilmenite} = a_{Fe}^{Fe-metal}$, and $fO_2 = \text{IW-1}$. When these constraints are applied, a_{TiO2}^{melt} ranges from 0.45 to 0.65 for respective temperatures from 900 to 1150 °C (EA-1).

For comparison, Crow et al. (2017) calculated lower a_{TiO2}^{melt} values from 0.1 to 0.2. These low values were based on MELTS simulations of KREEP basalt evolution along the liquid line of descent. Crow et al. (2017) noted that such low a_{TiO2}^{melt} values result in zircon crystallization temperatures in excess of 1250 °C, which were deemed to be unrealistic, after comparison with zircon saturation models (Boehnke et al., 2013). Crow et al. (2017) therefore shifted a_{TiO2}^{melt} to a preferred value of ~0.3, to yield better agreement with expected temperatures from zircon saturation thermometry.

Some general constraints are also possible for the silica activity of the melt (a_{SiO2}^{melt}; standard state relative to quartz saturation). The minimum possible value for silica activity in which zircon is stable is dictated by the reaction:

$$ZrO_2(bdl/zirconia) + SiO_2(melt) = ZrSiO_4 \quad (4)$$

In this case, silica activity is constrained by the presence of zirconia/baddeleyite and zircon. Using the thermodynamic data from Robie and Hemingway (1995), Eq. (4) yields an a_{SiO2}^{melt} of ~0.45 at 1150 °C (see EA-1). Lunar mineralogical observations provide additional constraints. If zircon-producing melts saturate in ZrO_2 first, followed by the onset of zircon saturation, it would be common to observe zircon armoring ZrO_2. This is only rarely observed, and such features are typically associated with morphologies attributed to impact-related shock features (e.g., Grange et al., 2013; Crow et al., 2017). Because this is the exception rather than the rule, the vast majority of zircon crystallization environments must have a silica activity larger than that calculated by the presence of co-existing ZrO_2 and zircon. On the other end of the spectrum, quartz monzodiorite clasts also contain zircon (e.g., Meyer et al., 1996) and therefore define the upper limit on silica activity as unity. Together, these observations yield a_{SiO2}^{melt} from >0.45 to 1. Crow et al. (2017) estimate a_{SiO2}^{melt} from 0.5 to 0.7, based on MELTS modeling for different candidate lunar source melt compositions, in agreement with the simple analysis presented here.

Overall, we expect a_{TiO2} and a_{SiO2} to have sub-unity values that are broadly comparable. If a_{TiO2} and a_{SiO2} are equal, this scenario results in a compensatory effect for the calculated Ti-in-zircon temperature (Ferry and Watson, 2007). Thus, the probable range of values for a_{TiO2} is from 0.45 to 0.65 and a_{SiO2} from >0.45 to 1. We anticipate that unity a_{SiO2} values are the exception, rather than the rule. We assume that a_{SiO2} and a_{TiO2} are broadly equal, and so no net activity correction is made for the calculated temperatures. If $a_{TiO2} = 0.45$ but the a_{SiO2} is 1 (or vice versa), the calculated Ti-in-zircon temperature will change by *ca.* 100°, but this scenario is considered to be an extreme case. More commonly we anticipate calculated temperatures to be within ~70° of the true values, reflecting an absolute difference of silica and titania activities of <0.3, based on the analysis presented here and MELTS models from Crow et al. (2017).

For the trace element data that follow, we consider three different ppm Ti (temperature) groups of 14–50 ppm (776–923 °C), >50–100 ppm (>923–1020 °C), and >100–194 ppm (>1020–1129 °C). The six zircons in the lowest temperature group have chemical characteristics that are largely distinct from other grains. The other two groups each define a ca. 100° temperature range, similar to the maximum estimated temperature uncertainty. Moreover, >50 ppm zircons exhibit some evidence for a bimodal distribution, with a division of the two modes at ~100 ppm Ti (Fig. 3), commensurate with our temperature-based group divisions.

4.3. Trace elements (REEs + P, U&Th) in zircon

After SIMS analyses, the data were checked for signs of contamination. Despite our efforts to carefully document the surface before SIMS measurements, there were a handful of analyses that appear to be chemically anomalous, possibly due to sputtering into sub-surface inclusions in lunar zircons (cf. Crow et al., 2017). Contaminated analyses were detected through examination of block data, and by a comparison of the light-REE to the middle-REE concentrations. Highly irregular or enriched LREE contents, relative to the middle REEs, are considered incompatible with zircon chemistry thus indicating probable contamination (e.g., by microscopic inclusions) or alteration (Bell et al., 2016). Of the 80 zircons measured, four are not considered further, though a plot of these chondrite-normalized patterns can be found in the supplementary information (EA-1).

We present zircon chondrite-normalized REE patterns grouped by zircon crystallization temperature (Fig. 4). Grains from ~776 to 923 °C have the largest average Σ[REE] of ~2700 ppm (Fig. 4a). The two high T groups (>923–1020 °C, and >1020–1129 °C) yield indistinguishable Σ[REE] of ~1300 ppm (Fig. 4b and c). A comparison (Fig. 4d), shows that the high T groups are in broad agreement with Apollo 14 zircon REE data previously collected by Crow et al. (2017). In contrast, the low T group (776–923 °C) shows some distinction with respect to Ce/Eu anomalies. Specifically, two zircon fragments with the lowest Ti contents (~14 ppm each) have Ce anomalies of ~7 and 16, compared to the average Ce anomaly ~1.5 for the rest of the samples (Ce anomaly = $Ce_N/\sqrt{[La_N \times Pr_N]}$, where concentrations have been normalized against chondrite). These two low T zircons also have the lowest Eu anomalies (0.016 and 0.012) of all grains investigated here. They are the only two zircons that yield trace element chemistry that is distinctly different. Otherwise, the REE patterns of all other zircons are characterized by similar general shape. Phosphorus contents in zircon (X_P^{zrc}) range from ~400 to 1800 ppm and do not exhibit any well-defined correlation with temperature or with REE(+Y)

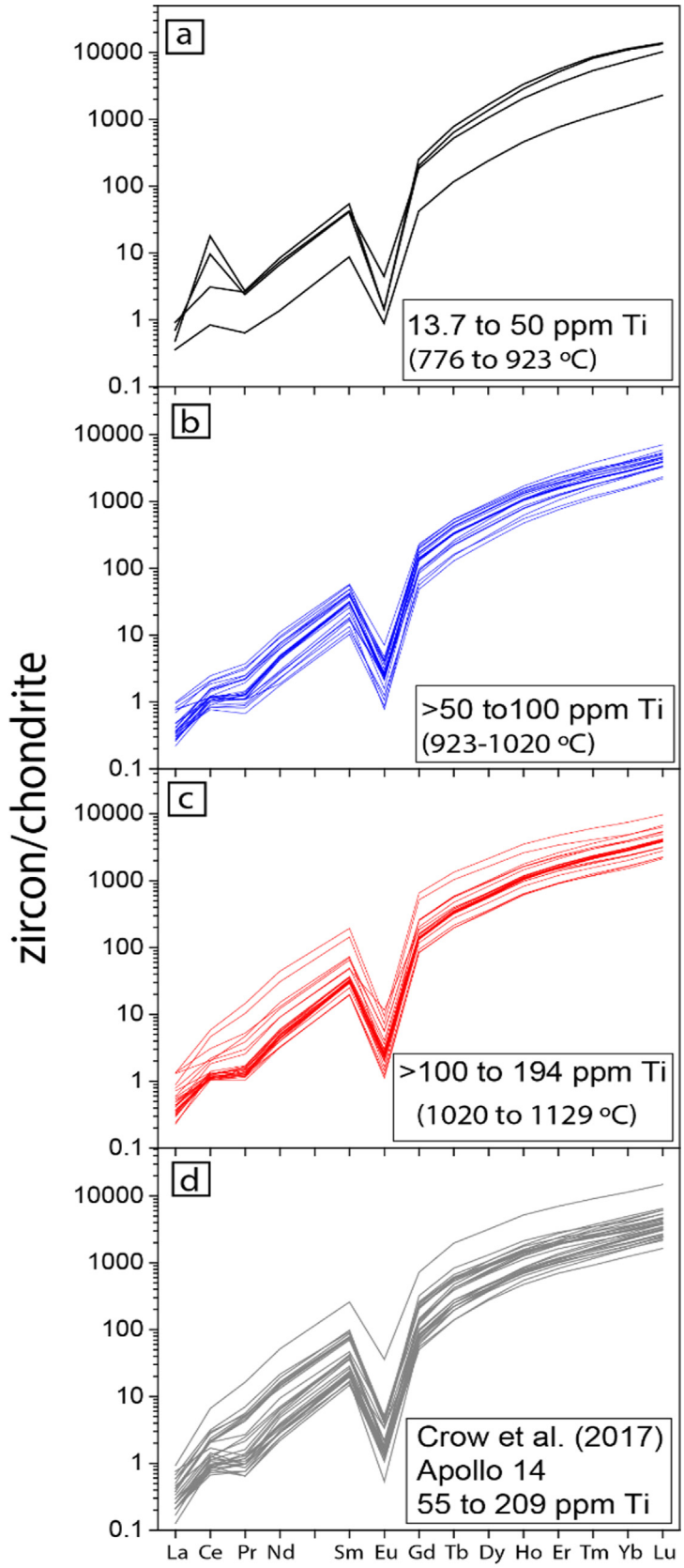

Fig. 4. Chondrite normalized REE patterns, grouped according to Ti content/crystallization T of zircon. (a) The average zircon Σ[REE] content (~2700 ppm) with < 50 ppm Ti is larger than Σ[REE] contents for the other two groups (~1300 ppm). The low Ti content zircons, specifically grains with ~14 ppm Ti, also have the largest Ce anomalies and the smallest Eu anomalies. (b and c) Zircon with Ti contents > 50 ppm have chemical characteristics that are indistinguishable. (d) Zircon patterns presented by Crow et al. (2017) compare well with the REE zircon chemistry presented in (b) and (c).

contents, a result that is further explored in the discussion (Section 5.2).

Zircons also incorporate tetravalent cations such as U, Th, and Hf, which have been considered possible indicators of source rock provenance. The Th/U ratio, for example, is used as a proxy to explore (terrestrial) provenance, as it tends to be lower in zircons which formed below the solidus (i.e., during metamorphism), when compared to magmatic crystals (e.g., Mojzsis and Harrison, 2002). Zircon $[U]_{initial}$, $[Th]_{initial}$, and $[Th/U]_{initial}$ are plotted against age (Fig. 5). The plots reflect initial actinide concentrations at the time of crystallization; that is, the values are corrected for radioactive decay. Zircon samples >4.2 Ga exhibit higher $[U]_{initial}$ and $[Th]_{initial}$ and more variation, compared to zircons with U-Pb ages in the 3.9–4.2 Ga interval. The older, pre-4.2 Ga grains also have a higher percentage of grains with low to moderate crystallization temperatures (squares and diamonds). There is no strong correlation between $[Th/U]_{initial}$ and age. The fact that this trend is not obvious, as opposed to when $[U]_{initial}$ and $[Th]_{initial}$ are plotted separately, shows that U and Th are (broadly) chemically coupled in the source melts.

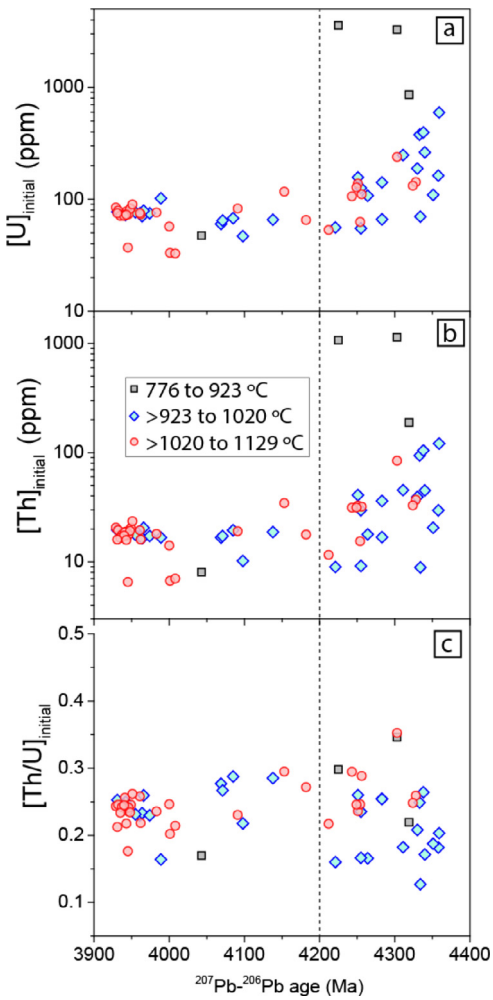

Fig. 5. (a) Zircon $[U]_{initial}$ (corrected for radioactive decay) showing a larger dispersion for >4200 Ma grains, when compared to zircons that crystallized later. The < 4 Ga grains have $[U]_{initial}$ from 37 to 102 ppm (average = 76 ppm), 4 to 4.2 Ga grains from 32 to 827 ppm (average = 111 ppm), whereas >4.2 Ga grains have $[U]_{initial}$ from 48 to 3577 ppm (average = 403 ppm). (b) Zircon $[Th]_{initial}$, with lower concentrations, show a similar trend as observed for $[U]_{initial}$. That is, the <4 Ga grains have $[Th]_{initial}$ from 7 to 24 ppm (average = 18 ppm), 4 to 4.2 Ga grains have $[Th]_{initial}$ from 7 to 117 ppm (average = 23 ppm), and >4.2 Ga grains have $[Th]_{initial}$ from 7 to 1135 ppm (average = 113 ppm). (c) Plot showing that the zircon $[Th/U]_{initial}$ remains mostly constant with time. Again for comparison, the < 4 Ga grains have $[Th/U]_{initial}$ from 0.16 to 0.26 (average = 0.24 ± 0.02), 4 to 4.2 Ga grains have $[Th/U]_{initial}$ from 0.14 to 0.3 (average = 0.24 ± 0.04), and >4.2 Ga grains have $[Th/U]_{initial}$ from 0.13 to 0.35 (average = 0.23 ± 0.06).

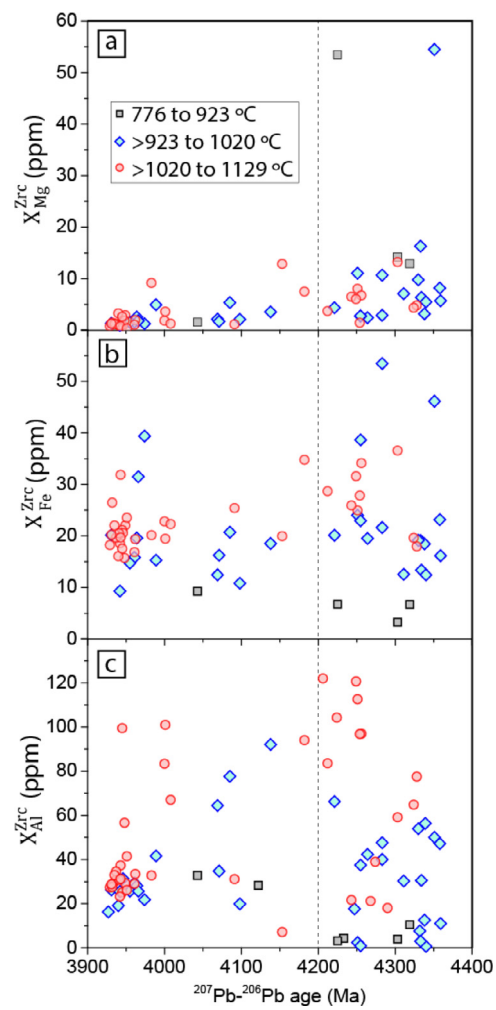

Fig. 6. Major rock-forming element concentrations in zircon plotted as a function of age. While there are no obvious trends between concentration and age, there is a larger range in values for the pre-4.2 Ga zircon suite. (a and b) Mg and Fe contents in zircons which range from ~0.2 to 55 and ~3 to 53 ppm, respectively, are interpreted to be robust zircon structure concentrations free of contamination. (c) The X_{Al}^{Zrc} range from 0.7 to ~122 ppm for grains over the entire range of ^{207}Pb-^{206}Pb ages (4.36–3.93 Ga).

4.4. Major rock-forming elements incorporated into zircon

We investigate concentrations of major rock-forming elements (Mg, Fe, and Al) incorporated into zircon as tracers of petrogenesis (Fig. 6; see EA-2 for tabulated data). The major elements Fe, Mg, and Al are incompatible in zircon, when compared to heavy REEs or Th/U/Hf, though they have a more direct relationship to the magma composition. To be consistent with the above trace element results, the four analyses that were rejected on the basis of contamination discovered in REE data were also removed from consideration here. As noted in the methods, Al + Ti were measured in a separate analytical session. Given that X_{Al}^{Zrc} has not been used previously for insights into lunar zircon petrogenesis, replicate analyses of Al (and Ti) were made for most of the grains. Very little intra-grain $X_{Al,Ti}^{zrc}$ variation was detected (typically < 5%), and so the averages of replicate grain analyses are reported. For all zircons studied aluminum concentrations, X_{Al}^{Zrc}, range from 0.7 to 122 ppm. The X_{Mg}^{Zrc} and X_{Fe}^{Zrc} range from ~0.2 to 55 and ~3 to 53 ppm, respectively, but with no correlation between X_{Mg}^{Zrc} and X_{Fe}^{Zrc}. The highest X_{Fe}^{Zrc} reported here is ~50 ppm, whereas 400 ppm Fe was a cutoff threshold for rejection of other trace element data (Crow et al., 2017) based on previous studies (Wopenka et al., 1996). The ranges for Mg, Fe, and Al concentrations in pre-4.2 Ga zircons are larger than in grains <4.2 Ga, in agreement with similar observations made for trace element concentrations.

There does not seem to be an obvious correlation with X_{Mg}^{Zrc} and temperature. The X_{Fe}^{Zrc} and X_{Al}^{Zrc}, on the other hand, show temperature dependent behavior that is clearer when plotted directly as such. This is explored in more detail in the discussion along with a thermodynamic treatment, where the goal is to use these concentrations to constrain melt composition.

5. DISCUSSION

5.1. Zircon U-Pb geochronology: robust ages alone do not define provenance

The reliability of chemical information from any sample of this antiquity (>3.9 Ga) must be critically examined. The mere survival of a mineral with apparent origins in primordial lunar environments does not mean that the mineral chemistry – including the age – was fully or even partially preserved (e.g., Borg et al., 2015; Dygert et al., 2017). Fortunately, crystalline zircon can preserve primary U-Pb ages through secondary heating due to the very high closure temperature of its U-Pb system. A zircon with a radius of 100 μm, for example, would lose only ~5% of its Pb if it were heated to 1100 °C for 10^3 years (Cherniak and Watson, 2000). Checks for zircon age disturbances are also possible though assessment of U-Pb concordance; our samples are almost all concordant, once errors are taken into account (EA-2). Thus, we interpret the ^{207}Pb-^{206}Pb ages to be representative of igneous crystallization.

However, the type of igneous melt, and the nature of its generation, is a matter of uncertainty. A zircon could represent crystallization from a fractionated magma that intruded into the primordial crust. The pre-4.0 Ga grains, for example, may represent a mixture of melt-generating processes related to lunar magma ocean differentiation, formation of Mg-suite rocks, and/or products of urKREEP-sourced melts. Other dating methods (e.g., Sm-Nd, Pb-Pb model ages) of rock clasts have yielded apparent age range overlaps for the Mg-suite rocks, FAN clasts, and the urKREEP reservoir (Borg et al., 2015; Snape et al. 2016a). These overlaps may indicate that these rocks were being generated contemporaneously, or that age information is only partially preserved through subsequent thermal processing of these ancient rock fragments (e.g., Borg et al., 2015; Dygert et al., 2017).

Zircon crystallization from impact-generated igneous melts add additional challenges. There are several possibilities of pre-Nectarian impact ejecta that could have reached the Apollo 14 landing site (e.g., Stoffler, 2006; Grange et al., 2011). For instance, Petro and Pieters (2008) predict that approximately ~1 km of South Pole Aiken basin ejecta covered the Apollo landing sites. In addition, samples from the Apollo 14 landing site contain significant material associated with the Fra Mauro formation thought to be formed by the Imbrium impact (e.g., Papanastassiou and Wasserburg, 1971; Stadermann et al., 1991). Merle et al. (2014) reported geochronology from 14311 Ca-phosphates from impact melt breccias, which yield an average ^{207}Pb-^{206}Pb age of ~3.94 Ga. This age is similar to the ^{207}Pb-^{206}Pb age of 3.93 Ga obtained from Ca-phosphate grains in Apollo 14 impact breccias 14305, 14306, and 14314 which were interpreted as the age of the Imbrium impact (Snape et al., 2016b). Hopkins and Mojzsis (2015) reported 14311 zircon ages of 3.93 and 3.95 Ga with poikilitic/granular textures, also interpreted as impact related. It is thus possible that <4.0 Ga zircon fragments analyzed here were formed in an impact melt (e.g.,

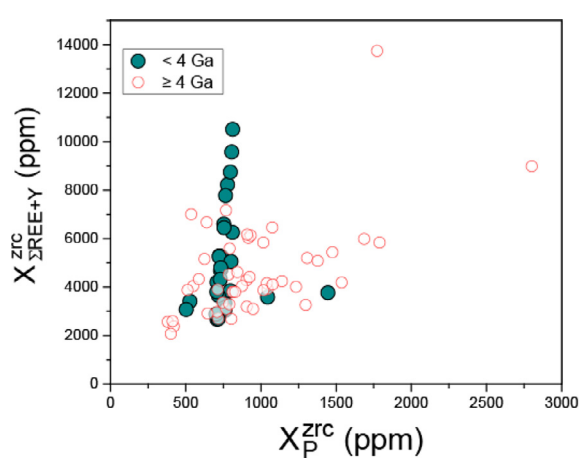

Fig. 7. Plot of $X^{zrc}_{\Sigma REE+Y}$ against X^{zrc}_{P} (both in ppm) showing a complex relationship. The array of near-vertical points may be due to X^{zrc}_{P} partitioning that is dominated by P_2O_5-buffered melt (via merrillite or apatite) in preference to the "xenotime"-type substitution ($^{(VIII\text{-}fold)}ZrSiO_4 \leftarrow\rightarrow {}^{(VIII\text{-}fold)}REEPO_4$). No correlation between P and Al was observed, and so there is no evidence to support $Al^{3+} + P^{5+} \rightarrow 2Si^{4+}$ as a substitution mechanism (EA-1).

Imbrium), though it is still less certain if they crystallized from a broadly monolithic remelted rock, preserving the original rock composition, of if several rocks re-melted, creating an entirely new composition. Pairing age information with appropriate trace element investigations are required to explore early igneous crystallization in the lunar crust.

5.2. Rare earth element (REE) patterns and phosphorus

Lunar zircon REEs patterns, have long been targeted as a tool to explore lunar melt source characteristics (e.g., Hinton and Meyer, 1991; Taylor et al., 2009). Nemchin et al. (2010) proposed four "types" of lunar zircon REE patterns, arguing that they represent trace element variations in residual melts capable of zircon saturation, rather than differences in melt sources. Hopkins and Mojzsis (2015) inferred that various REEs patterns reflected diversity within the melt source. Recently, Crow et al. (2017) argued that many of the REE pattern differences observed were due to contamination of analyses by small-scale inclusions; once this was taken to consideration, a broadly uniform pattern was observed (e.g., Fig. 4d). Crow et al. (2017) argued for a generally similar melt source, given constraints imposed by zircon REE patterns alone.

The observations of Crow et al. (2017) are broadly consistent with ours, when considering the REEs only (as evidenced by little variation in the REE patterns; Fig. 4). Another potential tracer of melt composition is the P content in zircon (X_P^{zrc}); it is plausible that grains crystallizing from a KREEP-like system would have higher X_P^{zrc} than those formed in other lunar magmas. Residual melts of the global lunar magma ocean were enriched in K, REEs, and P, (Warren and Wasson, 1979). This is in addition to other incompatible elements, like Zr, making mamas derived from urKREEP possible source melts for some zircons. Using the trace element data collected thus far, there is no correlation between X_P^{zrc} and T (EA-1). However, some interesting features are observed when X_P^{zrc} are plotted against $X_{\Sigma REE+Y}^{zrc}$ (Fig. 7).

In particular, the near-vertical data array for <4 Ga grains shows a clear decoupling of X_P^{zrc} from $X_{\Sigma REE+Y}^{zrc}$; that is, X_P^{zrc} is not strongly controlled by the substitution of REE + P for Zr + Si. In this case, it is possible that P_2O_5-bearing phases – such as apatite or merrillite – buffer the melt P_2O_5 activity, thereby constraining X_P^{zrc}. When considering ≥4.0 Ga grains only, there is a weak correlation between $X_{\Sigma REE+Y}^{zrc}$ and X_P^{zrc}, indicating that the "xenotime"-type substitution ($^{(VIII\text{-}fold)}ZrSiO_4 \leftrightarrow {}^{(VIII\text{-}fold)}REEPO_4$) does play a (small) role. It is also probable that the wide range in $X_{\Sigma REE+Y}^{zrc}$ values reflect local-scale trace element heterogeneities in the melt or non-equilibrium uptake, even though the overall REE pattern shown for most samples – presented in Fig. 4 – remains similar. Even if the origins of many of these grains are related to melting of an urKREEP source, establishing possible differences in urKREEP source(s), other magma types, or impact-derived melts is not straightforward based only upon the $X_{\Sigma REE+Y}^{zrc}$ and X_P^{zrc} data. Moreover, (terrestrial) impact grown zircons yield REE signatures similar to target rock zircons, making it difficult to identify zircons formed in impact melt sheets by using REE investigations only (Wielicki et al., 2012). While we recognize that REE patterns have value as discussed in past studies (e.g., Nemchin et al., 2010; Hopkins and Mojzsis, 2015), our observations place limits on what can be learned about melt composition from REEs + P alone. Thus, these elements do not provide the link to major element melt characteristics that we are after here.

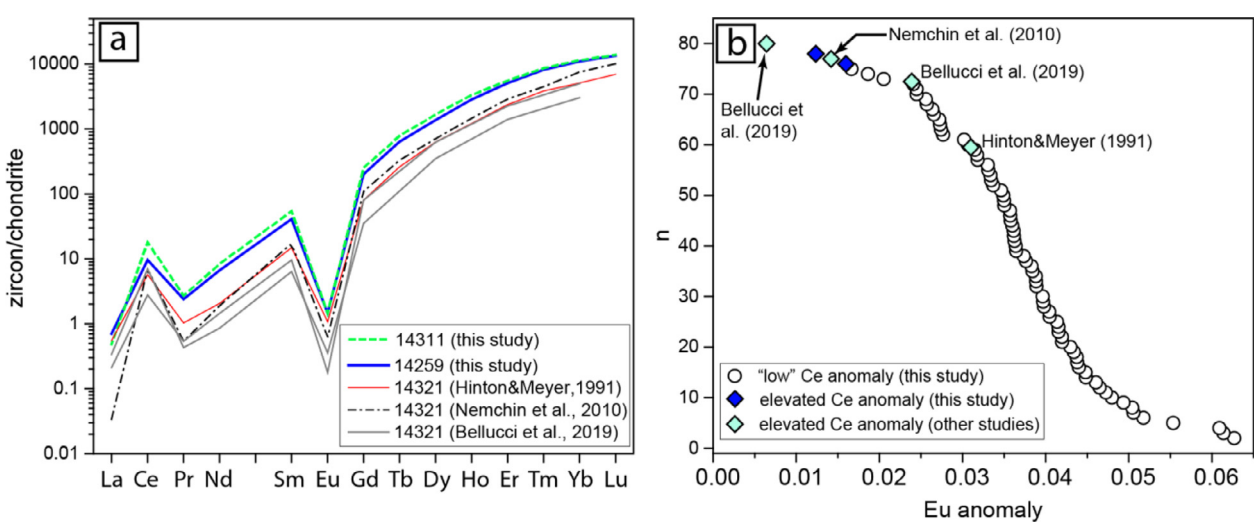

Fig. 8. (a) Summary of new data and other lunar zircons with notable Ce anomalies. The anomalies are calculated by $Ce_N/\sqrt{(La_N \times Pr_N)}$ where concentrations have been normalized against CI chondrite. Note that Hinton and Meyer (1991) reported an apparent Ce anomaly of ~8, though they cast doubt on the robustness of the analyses. The REE pattern of Nemchin et al. (2010) contained the steepest chondrite-normalized REE pattern, with the lowest LREE and the highest HREE presented as zircon, referred to in their contribution as "type-4." (b) Rank-order plot of zircon Eu anomalies; those with notable Ce anomalies from (a) are indicated. One Eu anomaly of 0.12 is not shown. Europium anomalies are calculated by $Eu_N/\sqrt{(Sm_N \times Gd_N)}$ where concentrations have been normalized against CI chondrite.

5.2.1. Unusual Ce anomalies

Almost all REE patterns have a similar shape to those reported by Crow et al. (2017). The exceptions to this generality are two grains that crystallized <800 °C (Fig. 4a) and display clear positive Ce anomalies. Indeed, while lunar zircons with crystallization temperatures >923 °C have Ce anomalies of 1.5 ± 0.3 (1 s.d.), those two sub-800 °C grains yield Ce anomalies of ~7 and ~16.

Distinctly higher Ce anomalies in lunar zircon have been documented in other studies too (Hinton and Meyer, 1991; Nemchin et al. 2010; Bellucci et al., 2019). Zircons from Apollo sample 14321 were found with high Ce anomalies (~8–52), with ages of 3.96–4.01 Ga (Hinton and Meyer, 1991; Nemchin et al. 2010; Bellucci et al., 2019). In cases where Ti-in-zircon thermometry has been conducted, prominent Ce anomalies are accompanied by "low" crystallization temperatures that range from 770 to 810 °C, (for equal titania and silica activities), whereas the average crystallization temperatures for lunar zircons are centered around ~1010 °C. The higher Ce anomalies and lower crystallization temperature also means they bear some resemblance to REE patterns of terrestrial zircons (Nemchin et al., 2010; Bellucci et al., 2019). These zircons may have crystallized under volatile-present conditions, as ~800 °C is below the dry granite and basalt solidus.

All prior data from Apollo sample 14321 are plotted (Fig. 8) along with our new data from 14259,511 and 14311,58. Our data marks the first occurrence of such low T zircons (and high Ce anomalies) outside of sample 14321 (Fig. 8a). The large positive Ce anomalies generally correlate with large negative Eu anomalies (Fig. 8b). The zircons with the 4 largest negative Eu anomalies, indicative of an extreme depletion of Eu in the melt due to feldspar fractionation (e.g., Trail et al., 2012), have the largest positive Ce anomalies. Our Apollo 14 samples are distinctive for two reasons. First, our results show that zircons with prominent Ce anomalies are not unique to 14321; we have identified them in two other Apollo 14 samples. Second, ages for our prominent Ce anomaly zircons are 4225 and 4303 Ma, making them ~300 Myr older than ages reported for 14321 zircons. Thus, the processes producing these prominent Ce anomalies in lunar zircons are not unique to a specific time interval, though this raises a larger question about the origin of these grains. The preferred interpretation of Bellucci et al. (2019) is that the zircons from 14321 were derived from a terrestrial meteorite, based on analysis of Ti-in-quartz, Ti-in-zircon, Ce anomalies in zircon, and application of experimental calibrations (Ferry and Watson, 2007; Thomas et al., 2010; Trail et al., 2011b). If Bellucci et al. (2019) are correct, it is reasonable to suspect these other zircons are of terrestrial origin, which would mean that terrestrial fragments on the Moon would now be documented in two breccia samples (14311, 14321) and a soil sample (14259). On the other hand, however, if these samples are endogenous to the Moon, it implies the existence of moderately volatile igneous conditions at least sporadically over a long time frame (4.3, 4.22, and 4 Ga). Until more information is available, our preferred interpretation is that these samples are of lunar affinity. No matter their ultimate origins, these zircons crystallized at low temperatures from highly-fractionated volatile-rich magmas.

5.3. Heterogenous [Th] and [U], broadly homogenous Th/U in zircon

To explore the reasons of heterogenous $[Th]_{initial}$ and $[U]_{initial}$ in zircon (Fig. 5), we first present a conceptual model to help frame the discussion. If all melts have identical Th and U concentrations, X^{zrc}_{Th} and X^{zrc}_{U} should depend only on T. That is, the partition coefficient (e.g., $X^{zrc}_{Th}/X^{melt}_{Th}$), will reflect an exchange reaction between zircon and melt. This exchange reaction is characterized with an equilibrium constant K, which should be inversely related to T by the expression $\ln[K] = -\Delta G/RT$ (where ΔG is the Gibbs free energy of the reaction that defines actinide partitioning between zircon and melt, and R is the gas constant). Some evidence for an inverse relationship of $[Th]_{initial}$ and $[U]_{initial}$ with T is found in pre-4.2 Ga zircons when inspecting the low- middle- and high T-groups (squares, diamonds, circles; Fig. 5a and b). In general, however, the predicted trend is not observed, so other factors must be responsible for the detected heterogeneities. The two reasonable possibilities are: (i) this could be a local occurrence for each melt linked to saturation of other U- and Th-bearing phases; or (ii) this could be related to intrinsic $[Th]_{initial}$ and $[U]_{initial}$ variability in the source melts.

First, we explore the possibility that other U- and Th- bearing phases are responsible for the actinide heterogeneities observed in zircon. Many of the other phases-of-interest have different mineral-melt compatibilities of U vs. Th (e.g., apatite and merrillite). Thus, it is reasonable to consider the Th/U ratio in zircon as a proxy for what may be happening in the melt due to the crystallization of other phases. To first order, we see no evidence for wide variation in the $[Th/U]^{Zrc}_{initial}$. In addition, $[Th/U]^{Zrc}_{initial}$ is not sensitive to temperature across the suite of zircons (Fig. 9a). We further evaluated this by producing three $[Th/U]^{Zrc}_{initial}$ plots for each of the previously defined temperature groups (Fig. 9b). The low-, medium-, and high-T zircons yield average $[Th/U]^{Zrc}_{initial}$ values of 0.26 ± 0.08, 0.22 ± 0.04, and 0.25 ± 0.04 (1 s.d.), respectively.

This broad observation is somewhat surprising given that merrillite and apatite structurally accommodate Th and U, and thus warrants a closer look. Using the ion microprobe data for ~3.94 Ga apatite and merrillite from sample 14311 (Merle et al., 2014), $[Th/U]^{Apatite}_{initial} \approx 0.31$ and $[Th/U]^{Merrillite}_{initial} \approx 6.5$ were calculated. Assuming a $[Th/U]^{Melt}_{initial}$ of ~2 (Warren et al., 1983), merrillite crystallization will lower the Th/U of the melt, whereas apatite will increase the Th/U of the melt. While there is evidence that merrillite and apatite may have been present in the zircon melt environment at ~3.94 Ga, there is no evidence for a change in $[Th/U]^{Zrc}_{initial}$ at this time, when compared to older zircons found in 14311. Either merrillite and apatite were also present among the older zircon parent melts in similar modal abundances as the <4.0 Ga suite, or actinide

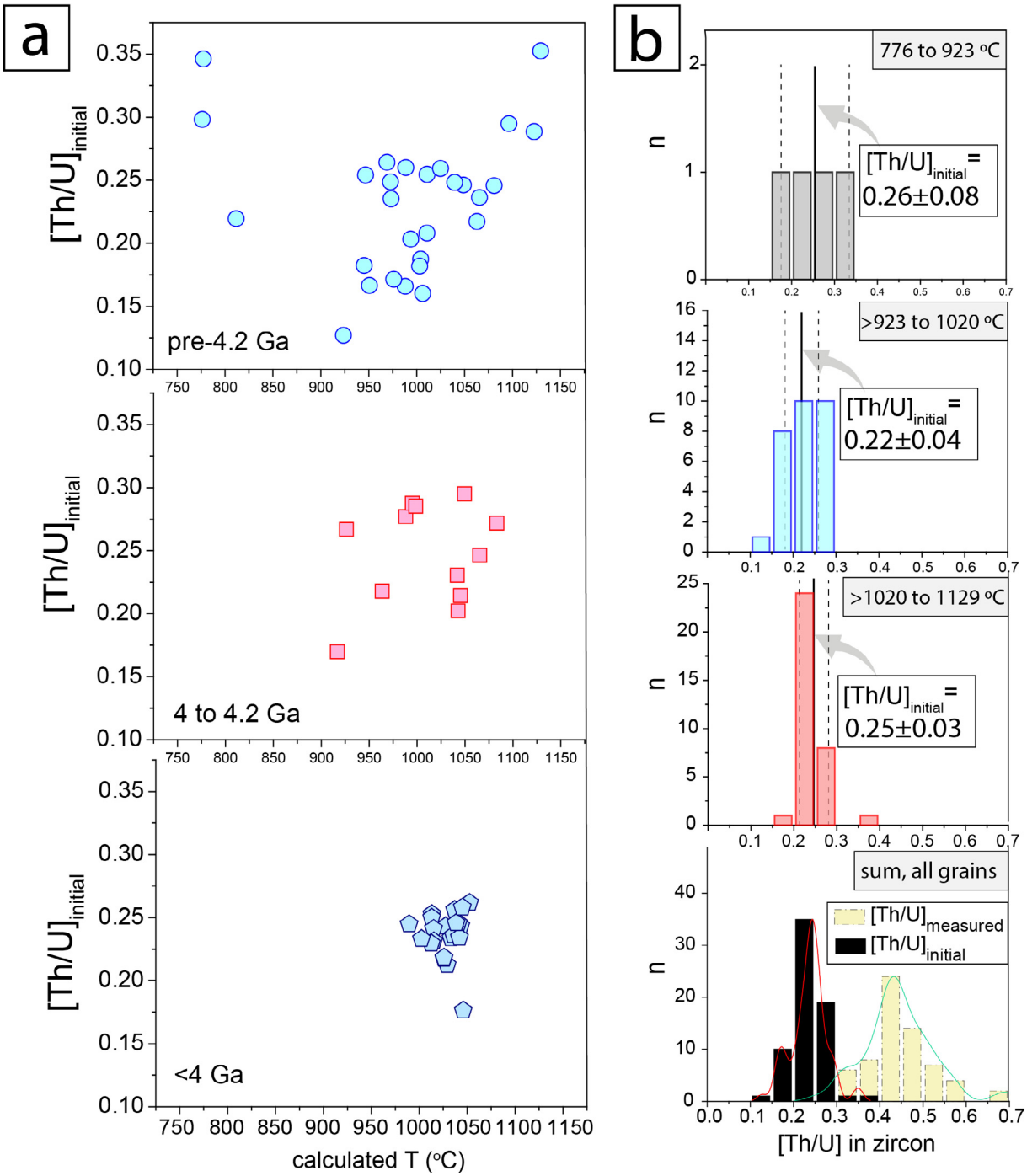

Fig. 9. (a) Zircon $[Th/U]_{initial}$ does not show a strong systematic relationship when plotted against temperature. (b) Based on the temperature groupings described in the text, zircon $[Th/U]_{initial}$ values for zircons are plotted in three histograms, showing no apparent change in this ratio with temperature. The bottom histogram shows zircon $[Th/U]_{initial}$, plotted with $[Th/U]_{measured}$. Correcting for radiogenic ingrowth shifts the distribution down to lower (initial) Th/U values. This correction also tightens the range, resulting in a smaller dispersion of the ratio. This tightening occurs because the correction to the $[Th/U]_{initial}$ ratio is a function of age, so the correction is not completely systematic over the ca. 500 Myr interval represented by the zircons.

fractionation in the melt is not sufficiently large to make a measurable impact on the actinide chemistry of co-existing zircon. It is also reasonable to expect that the frequency of accessory minerals and their proximity to other phases will dictate the local trace element environment. Major rock-forming phases, for example, could isolate accessory minerals so that there is limited chemical communication among accessory phases during the late stages of melt evolution. There does appear to be a lower $[Th/U]^{Zrc}_{initial}$ for some mid-T pre-4.2 Ga zircons (Fig. 9a), when compared to only

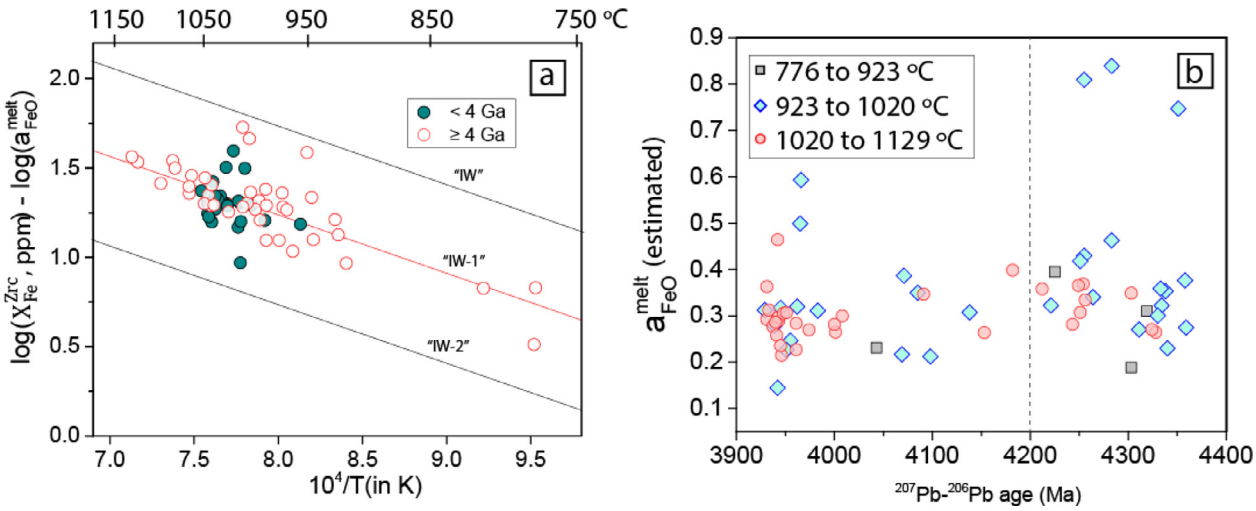

Fig. 10. Plot of $\log(X_{Fe}^{Zrc}, ppm) - \log(a_{FeO}^{melt})$ vs. 1/T with a global line fitted to all the data. The fit assumes an *average* oxygen fugacity of IW-1 as a point of reference, which in the presence of Fe-metal, is the same as $a_{FeO}^{melt} = 0.31$. The quotes demarking the oxygen fugacities in the graph (relative to IW) indicate that fO_2 is assumed. The other fO_2 values mark the location of the predicted X_{Fe}^{Zrc} for an fO_2 of IW ($a_{FeO}^{melt} = 1$) and IW-2 ($a_{FeO}^{melt} = 0.1$). (b) When corrected for the effect of temperature on solubility, predicted a_{FeO}^{melt} (estimated) values are broadly restricted. The three highest values are from the pre-4.2 Ga suite.

the high-T group of the same age, perhaps due to merrillite crystallization along this portion of the liquid line of descent. However, the lowest-T zircons in the pre-4.2 Ga group (Fig. 9a) also have $[Th/U]_{initial}^{Zrc}$ similar to the high-T zircons. To fully explain the data, an alternative is required.

The simplest model that explains the observations of variable $[Th]_{initial}$ and $[U]_{initial}$ of pre 4.2 Ga zircons is source melt heterogeneity of heat-producing elements U and Th (and likely K). While the chemical and physical processes operating on the Moon resulting in zircon-saturated melts yield highly variable $[Th]_{initial}$ and $[U]_{initial}$ in zircon, there is only limited evidence for processes that systematically fractionate Th from U. A plausible explanation for this result is that the pre-4.2 Ga zircon parent melts record variable degrees of urKREEP assimilation/contamination, and/or different urKREEP sources. The majority of urKREEP and radioactive elements are believed to be largely concentrated in the PKT terrane (e.g., Laneuville et al., 2013, 2018), though trace element heterogeneities of FAN clasts point to variable trace element enrichments in the lunar anorthosite parent magmas as well (e.g., Warren et al., 1983; Pernet-Fisher et al. 2019).

On the other hand, the $[Th]_{initial}$ and $[U]_{initial}$ of <4.2 Ga grains are largely homogenous. We interpret this as evidence that melts produced after 4.2 Ga were derived from a more homogenous source or that these later samples reflect lithospheric mixing and homogenization (i.e., remelting). That is not to say that the entire <4.2 Ga melt suite(s) were homogeneous, but the portion that was sampled by zircon during crystallization appears to have similar melt actinide composition characteristics.

5.4. Fe, Mg, Al in zircon

Zircon trace element data discussed above support the view that melts were more heterogeneous before 4.2 Ga then afterwards. This section explores the extent to which major rock-forming elements can help to identify the characteristics of various zircon-producing magma sources. We use this information, along with thermodynamic modeling, to help place zircon genesis in the broader context of endogenous vs. exogeneous lunar melt generation during the pre-Nectarian (~≥3.92 Ga).

5.4.1. Fe, Mg in zircon

We explore X_{Fe}^{Zrc} by assuming that Fe^{2+} is incorporated into lunar zircon, and that Fe-metal is present in the crystallization environment (Section 4.2). The presence of Fe-metal (e.g., Ryder 1976; Taylor et al., 1980) along with the oxygen fugacity constrains the activity of $Fe^{2+}O$ in the melt (a_{FeO}^{melt}) by the following simple reaction:

$$Fe(metal) + 1/2O_2 = FeO(melt) \quad (5)$$

With Fe-metal present, a constrained fO_2, and the equilibrium constant for Eq. (5), the a_{FeO}^{melt} can be calculated. Using an fO_2 of IW-1 (Section 4.2), and the equilibrium constant for this reaction (O'Neill, 1987), we calculate a_{FeO}^{melt} (relative to wüstite) to be 0.31. This estimate agrees with work conducted by Sato et al. (1973), who estimated a_{FeO}^{melt} values of 0.25–0.35 for Apollo basalts. The next step is to relate X_{Fe}^{Zrc} to a_{FeO}^{melt}, which is still plagued with uncertainty because the equilibrium reaction governing the entry of Fe^{2+} into zircon is not known, and there are no systematic studies which have explored X_{Fe}^{Zrc}. We can nevertheless make some useful generalizations.

We assume that Fe substitutes in zircon in a regular predictable fashion and that Fe^{2+} was incorporated into zircon with an *average* a_{FeO}^{melt} equal to 0.31. Recall that the latter constraint requires an fO_2 of IW-1, and the presence of Fe-metal. If these assumptions are correct, a plot of log (X_{Fe}^{Zrc}, ppm) vs. 1/T plot should yield a linear relationship. In detail, it is more accurate to express the y-axis as log

(X_{Fe}^{Zrc}, ppm) – log(a_{FeO}^{melt}), which takes into consideration changes in X_{Fe}^{Zrc} with the a_{FeO}^{melt} (see EA-1). All data are plotted as log(X_{Fe}^{Zrc}, ppm)–log(a_{FeO}^{melt}) vs. 1/T, (assuming $a_{FeO}^{melt} = 0.31$) which shows broad confirmation of the predicted trend (Fig. 10).

For illustration, we can recalculate the location of this line at a "maximum" $a_{FeO}^{melt} = 1$ (i.e., at IW) and at $a_{FeO}^{melt} = 0.1$ (IW-2) according to Eq. (5). While these limits imposed are general, it allows us to make several key observations. If an average fO_2 of IW-1 is a reasonable starting point, the upper "IW" line defines the maximum $X_{Fe(2+)}^{Zrc}$ (ppm) in zircon. If values plot above this line, it means that our assumption of a systematic incorporation mechanism of Fe in zircon is invalid, and/or our estimated starting fO_2 (IW-1) is incorrect. Therefore, there is no obvious indication that our assumptions have been violated. Except for a handful of data, we see little evidence for variation in the estimated a_{FeO}^{melt} for these zircon parent melts, as shown in Fig. 10b. This implies that this aspect of melt composition is, for the most part, broadly similar for zircon-saturated lunar melts at the Apollo 14 site.

In contrast to Fe, Mg exhibits little dependence upon temperature. The reason why T trends are observed in Fe but not Mg is not entirely clear, but one possibility is that many Mg-bearing phases that could impose buffered MgO activities on samples become armored with FeO below ~1100 °C, thereby chemically isolating these phases from communication with the melt (and zircon). In summary, the main observation from our analyses and calculations indicate there was relatively little variation in a_{FeO}^{melt} producing lunar zircons. More direct confirmation of this will require experimental studies.

5.4.2. Al in zircon reveals diverse melt compositions

In general, investigations of Al in zircon are further advanced than Mg or Fe. This is because the variables that control Al substitution in zircon are better understood. Trail et al. (2017) measured X_{Al}^{Zrc} in terrestrial zircons from 19 geographically and petrologically diverse rocks. These rocks span a key compositional boundary of magmas, defined by whether Aluminum Saturation Index (ASI; the molar ratio of Al_2O_3/(CaO-Na_2O-K_2O)) is larger or smaller than unity. Rocks with ASI < 1 are classified as metaluminous whereas rocks with ASI > 1 are referred to as peraluminous. Zircon from peraluminous rocks (ASI = 1.03–1.6) yield X_{Al}^{Zrc} about an order of magnitude higher than grains from metaluminous rocks (ASI = 0.88–0.99). This demonstrates X_{Al}^{Zrc} has potential as an indicator of melt composition.

Experimental studies have also been conducted, largely with terrestrial applications in mind (Trail et al., 2011; Wang and Trail, 2019). These results are nevertheless useful for context here. For example, it was demonstrated that trivalent Al can substitute into the zircon structure along with H to replace Si (Trail et al., 2011). More recently, zircon-melt Al partitioning experiments were reported for hydrous felsic melts in the SiO_2-Al_2O_3-Na_2O-K_2O-CaO-ZrO_2-H_2O system (Wang and Trail, 2019). Four compositions with ASI values ranging between 0.50 and 1.3 were prepared, including one peralkaline (Al_2O_3/[Na_2O-K_2O] < 1), one metaluminous, and two peraluminous mixtures. Zircons were synthesized in a piston cylinder device at 1100–1400 °C, 1 GPa, with 10 wt% H_2O added to the rock mixes. Two main observations were made. First, X_{Al}^{Zrc} was shown to be positively related to melt ASI for a given temperature. Second, for each composition, log(X_{Al}^{Zrc}, ppm) is proportional to 1/T. We use these experimental observations to guide our interpretation of lunar X_{Al}^{Zrc}.

We start by writing out a candidate equilibrium reaction. Stoichiometric zircon is comprised of tetravalent cations Si^{4+} and Zr^{4+}, so the entry of Al^{3+} into zircon requires charge balance:

$$ZrSiO_4(zircon) + 1/2Al_2O_3(melt) + 1/2H_2O(melt) = Zr[AlH]O_4(zircon) + SiO_2(melt) \quad (6)$$

Another plausible reaction involves the replacement of $2Si^{4+}$ for Al^{3+} and P^{5+}, which is not preferred here because there is no evidence of correlation between P and Al in zircon (EA-1). On the other hand, FTIR spectra of experimental zircon show that H is coupled with Al (Trail et al., 2011a). The expression ($Zr[Al^{3+}O(OH)]O_2$) may be a slightly more accurate structural representation of this substitution, though we choose $Zr[AlH]O_4$ for simplicity. The activity of H_2O (a_{H2O}), is also a function of fO_2, because of the following equilibrium reaction:

$$H_2 + 1/2O_2 = H_2O \quad (7)$$

where, for a given water content, lower fO_2 will lower the activity of H_2O (and OH) of the system. For a lunar melt with ~100 ppm H_2O or more (e.g., Hauri et al., 2011) and an fO_2 of IW-1, equilibrium experiments predict a molar ratio of ~0.05 for H_2/[$H_2 + H_2O$] in the lunar crust (Hirschmann et al., 2012). That is, ~95% of H would be present as H_2O. The same experimental study also predicts that the fraction of H_2O increases as the concentration of H in the melt decreases, assuming pressure and fO_2 remain fixed.

The equilibrium constant for Eq. (6) – assuming $ZrSiO_4$ is essentially pure and thus its activity is equal to unity – becomes:

$$K_{Al-H} = \frac{[a_{Zr[AlH]O4}^{zrc}] \times [a_{SiO2}^{melt}]}{[a_{Al2O3}^{melt}]^{1/2} \times [a_{H2O}^{melt}]^{1/2}} \quad (8)$$

Making the following assumption that:

$$a_{Zr[AlH]O4}^{zrc} \approx [X_{Al}^{zrc}, ppm] \times k_1 \quad (9)$$

where k_1 is the Henry's Law constant that relates $a_{Zr[AlH]O4}^{Zrc}$ to $X_{Zr[AlH]O4}^{Zrc}$ and the factor that converts $X_{Zr[AlH]O4}^{Zrc}$ to X_{Al}^{Zrc} (in ppm). Substituting Eqs. (8) and (9) into the expression log (K) = –ΔG/[2.303RT] = –ΔH/[2.303RT] + ΔS/[2.303R], where ΔG, ΔH, and ΔS are the respective free energy, enthalpy, and entropy changes for the reaction, R is the ideal gas constant, and T is temperature (in K), yields the following:

$$\log[X_{Al}^{Zrc}, ppm] + \log(k_1) = -\frac{\Delta H}{2.303RT} + 1/2\log[a_{Al2O3}^{melt} \times a_{H2O}^{melt}] - \log[a_{SiO2}^{melt}] + \frac{\Delta S}{2.303R} \quad (10)$$

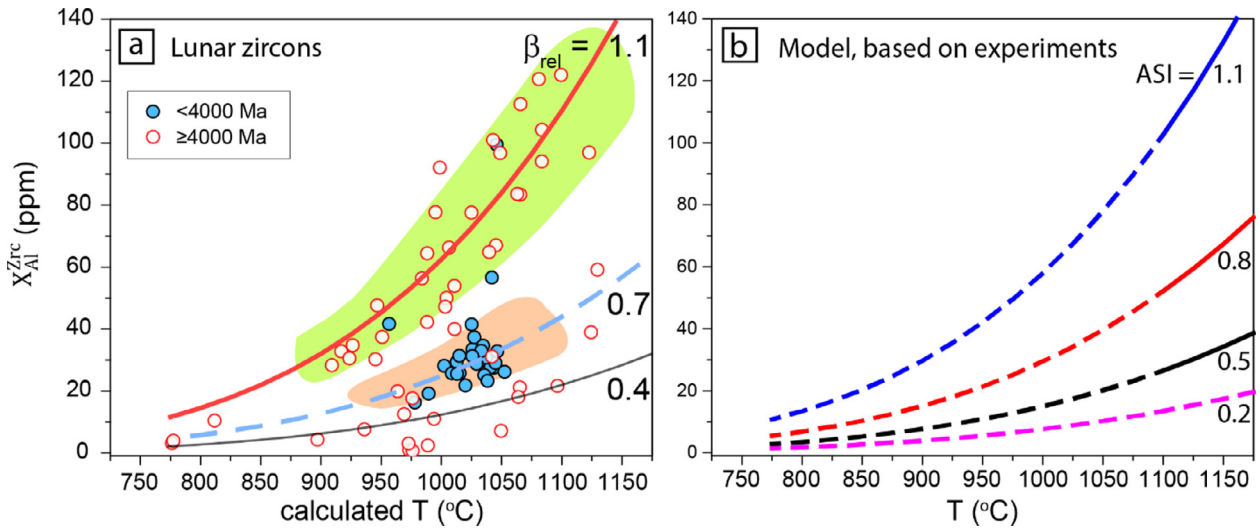

Fig. 11. (a) Plot of X_{Al}^{Zrc} vs. T, also with two shaded regions that encompass most of the data, which we hypothesize to represent broadly different melt compositions. Temperature is calculated though application of the Ti-in-zircon thermometer and the activity modeling presented in Section 4.2. The curves for β_{rel}, defined by Eq. (11), should be thought of as a parameter indicative of the *relative* compositional differences in the melt, or more specifically the activities of key components. For example, increasing the alumina activity and water activity causes β_{rel} to increase. Increasing the silica activity causes β_{rel} to decrease. (b) Modeled X_{Al}^{Zrc} vs T for hydrous granitic melts (quartz undersaturated) with different ASI melt compositions (Wang and Trail 2019). The curves are calculated from the empirical relationship presented in (Wang and Trail, 2019). Experiments conducted in that study range from 1400 to 1100 °C; the dashed lines in (b) indicate an extrapolation beyond the experimental results.

where a_{Al2O3}^{melt} is the activity of alumina in the melt, etc. Eq. (10) predicts that as a_{Al2O3}^{melt} and a_{H2O}^{melt} increase, so should X_{Al}^{Zrc}, an expectation consistent with natural observations made on terrestrial samples. That is, it was demonstrated that rocks with higher ASI values – a parameter that is likely to be correlated to a_{Al2O3}^{melt} – also have higher X_{Al}^{zrc} (Trail et al., 2017). Moreover, zircons from metaluminous water-deficient (i.e., low a_{H2O}^{melt}) anorogenic-type terrestrial magmas have significantly lower X_{Al}^{Zrc} when compared to zircons found in metaluminous melts with similar ASI (Trail et al., 2017), also consistent with Eqs. (6) and (10). Eq. (10) also predicts that as a_{SiO2}^{melt} increases, a corresponding decrease in X_{Al}^{Zrc} will occur. Because we do not have the full complement of activity information, we express the interplay of these intensive variables as β_{rel}, a parameter expected to dictate the uptake of X_{Al}^{Zrc}:

$$\beta_{rel} \equiv 1/2\log\left[a_{Al2O3}^{melt} \times a_{H2O}^{melt}\right] - \log\left[a_{SiO2}^{melt}\right] \quad (11)$$

We note that a_{SiO2}^{melt} could be assigned a fixed value (e.g., see Section 4.2), and a modest value for a_{H2O}^{melt} (10^{-3}?) could be assumed to calculate a_{Al2O3}^{melt}, though at present we do not have the confidence needed to assign specific values to these variables for this suite of zircons. We therefore use β_{rel} as a parameter to quantify relative differences in the melt environment. We emphasize that this parameter could vary along the liquid line of descent, if the three variables that define β_{rel} change at different rates during cooling. Consider, for example, a system that becomes quartz-saturated that is not vapor (H_2O) saturated. Once quartz saturates, a_{SiO2}^{melt} is buffered by quartz, but a_{H2O}^{melt} may continue to change during cooling.

Eq. (10) can also be modified by using the enthalpy of reaction – or more specifically $\Delta H/2.303R$ – from Wang and Trail (2019) who conducted experiments to explore Al partitioning in zircon. Assuming that $\Delta S/[2.303R]$ and $\log(k_1)$ are constants, we define $k_2 = \Delta S/[2.303R] - \log(k_1)$. With all considerations, Eq. (10) becomes:

$$\log\left[X_{Al}^{Zrc}, ppm\right] = \frac{-4334 \pm 459}{T(K)} + \beta_{rel} + k_2 \quad (12)$$

Thus, with knowledge of X_{Al}^{Zrc}, T, and k_2, the differences in zircon source melts can be explored via β_{rel}. Note that β_{rel} is the *relative* variation of the activity relationships in Eq. (11). To explore the *relative* variation of the model activity relationship presented in Eq. (11), we assume a constant value of ~4.1 for k_2 (Wang and Trail, 2019). When better constraints are possible for $k_2 = \Delta S/[2.303R] - \log(k_1)$ though experimental characterization, β_{rel} will become an *absolute* value. We plot X_{Al}^{Zrc} vs. T; superimposed upon this, we show calculations using Eq. (12) with three illustrative β_{rel} values (Fig. 11a). This reveals clear evidence that compositional differences exist in lunar zircons that are derived from their parent melts. The empirically-modeled X_{Al}^{Zrc} values for melts with different ASI values, predicted by the experimental results of Wang and Trail (2019), are shown for comparison (Fig. 11b).

The correlation between T and X_{Al}^{Zrc} is evident in Fig. 11a, as is the clustering of data in certain regions of the graph. When considering what magmas could have formed these zircons, a few generalizations are possible. First, recall that increasing the alumina (and water) activity causes β_{rel} to increase. That is, for the same temperature, a melt with higher alumina activity will produce zircons with

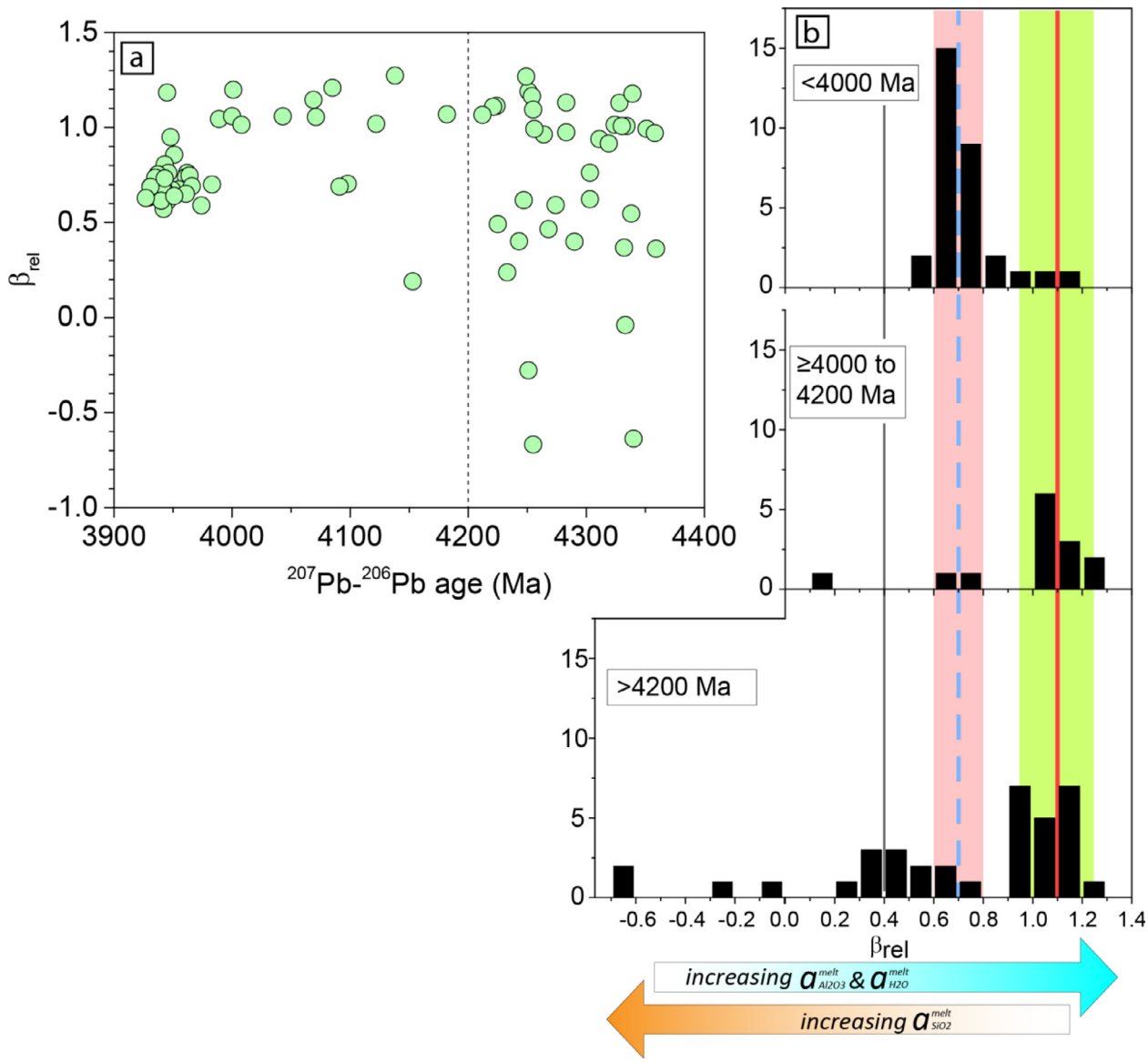

Fig. 12. (a) β_{rel} values for zircon – defined in Eq. (11) – and interpreted to be a proxy for melt composition plotted against age. The β_{rel} is solved for using the Ti-in-zircon crystallization temperature and experimental data from Wang and Trail (2019). See Sections 4.2, 5.4.2, and Eq. (12) for details. This parameter displays the greatest variation in pre-4.2 Ga zircons. (b) The histograms show β_{rel} for three different time intervals, which uncover differences in calculated melt compositions. The >4200 Ma samples have the most diverse melts, with potentially three distinct types ($\beta_{rel} = \sim1.1$, ~0.4, and <0). The arrows at the bottom of the figure indicate how changes in the intensive variables will change β_{rel}, a parameter which is positively correlated with X^{Zrc}_{Al}. An increase in a^{melt}_{Al2O3} (and a^{melt}_{H2O}) will lead to an increase in β_{rel}, whereas an increase in a^{melt}_{SiO2} will lead to a decrease in β_{rel}. The lines and shaded regions, taken from Fig. 11a, highlight the common melt types.

higher Al contents. On the other hand, increasing a^{melt}_{SiO2} causes β_{rel} to decrease, and therefore X^{Zrc}_{Al} to decrease.

5.5. Melt origins using the zircon β_{rel} model

We can assess the range of β_{rel} in lunar melts via Eq. (11) by assuming that a^{melt}_{SiO2} and a^{melt}_{H2O} are relatively restricted, which means that a^{melt}_{Al2O3}, is largely responsible for differences in calculated β_{rel} values. The resulting β_{rel} values are plotted against crystallization age in Fig. 12.

5.5.1. The origins of pre-4.2 Ga zircons based on β_{rel}

The two most abundant β_{rel} values range from about 0.2 to 0.7 (average = ~0.4) and from about 0.9 to 1.2 (average = ~1.1). If our model is correct, at least two different magma compositions are required. We discuss the origins of the high ~1.1 β_{rel} group first, which is also likely to have the highest ASI values. Zircons from this group were formed in high alumina activity environments and we consider three different models: (1) formation in FAN; (2) formation from fractionally crystallized Mg-suite magmatism; and (3) formation within impact melts.

Model 1 is a reasonable place to start because the most obvious high Al_2O_3 lunar terrane, constituting >50% of the present-day lunar surface, is the Feldspathic Highlands Terrane (FHT; Al_2O_3 ~29 wt%) which is believed to have formed during the earliest lunar differentiation as a flotation cumulate of ferroan anorthosite (FAN) from the magma ocean (e.g., Tompkins and Pieters, 1999; Jolliff et al., 2000). This FHT-like terrane was likely even more extensive on the near side of the Moon – both in terms of thickness and exposed surface area – before 4.2 Ga than is presently observed (e.g., Wieczorek et al., 2006). While zircons have been found in Apollo 14 anorthosite clasts 14321,16 (Nemchin et al., 2008), it is not likely that FAN was a common source for these zircons, due to a relatively restricted range of incompatible elements like Zr in FAN rocks (cf. Pernet-Fisher et al., 2019). Moreover, the ages of zircons contained within the clasts documented by Nemchin et al. (2008) only reach ~4.04 Ga. This is younger than even the youngest Sm-Nd ages reported for lunar anorthosites (Borg et al., 2015), calling into question the relationship of these zircons with the anorthosite clasts. We therefore consider this origin for ~1.1 β_{rel} zircons to be the exception.

In model 2 we consider the high β_{rel} zircon genesis during fractional crystallization of the Mg-suite rocks. The lunar highlands Mg-suite were plausibly formed when high temperature Mg-rich mantle-derived magmas assimilated with FAN and an urKREEP source (e.g., Shearer et al., 2006b; Elardo et al., 2011). We consider this model reasonable given that Mg-suite rocks satisfy two key criteria. First, Mg-suite rocks are enriched in incompatible elements required for zircon saturation. Second, the high-T Mg-rich magmas can plausibly assimilate high-Al_2O_3 FAN, which requires a significant heat source for fusion (Elardo et al., 2011). The magmas presumably undergo fractional crystallization during cooling in the crust to yield high β_{rel} zircon.

In model 3 we consider the formation of high β_{rel} zircon from impact melts. Because FAN rocks require significant energy to melt, the high β_{rel} zircons may represent crystals formed in very large impact melt sheets of the pre-Nectarian Moon (e.g., White et al., 2020). We speculate that some of the high β_{rel} grains were products of impact-generated melts. Aluminum-rich spinel anorthosites are predicted to form in impact-generated melts (Treiman et al., 2019), and these rocks seem to be more abundant than originally thought (Sun et al., 2017; Gross and Treiman, 2011). This suggestion notwithstanding, we propose that zircon with higher relative X_{Al}^{Zrc} (high β_{rel} values of ~1.1) are caused by parental melts that assimilated some plagioclase-rich crust. If correct, then inclusion of FAN rocks into lunar melts was apparently a common occurrence on the pre-4.2 Ga Moon.

The pre-4.2 Ga zircons with β_{rel} = ~0.4 may be derived from an urKREEP source with limited or no chemical interaction with FAN. This scenario should yield zircons, on balance, with lower β_{rel} values (i.e., lower X_{Al}^{Zrc} once temperature is taken into consideration; see Fig. 12). These zircons may be more direct reflections of re-melted urKREEP from early magma ocean differentiation (Warren and Wasson, 1979). Lunar zircons derived from KREEP basalts have long been considered to be the source for the majority of out of context grains (Taylor et al., 2009; Crow et al., 2017). This scenario may not be valid for all KREEP basalts. High Al_2O_3 (~19 wt%) Apollo 14 KREEP basalts may have obtained their chemical composition due to a more extensive assimilation of FAN material (Ryder and Bower, 1976; Snyder et al., 1995). We note that the two zircons with high Ce anomalies (Section 5.2.1) both fall in this group (β_{rel} = 0.49, 0.62). These two grains may record open system volatile-present mesostasis crystallization from an extremely fractionated basalt.

The small fraction of pre-4.2 Ga grains with β_{rel} values <0 (4 out of 37) appear distinct from the other two groups. Their crystallization temperatures fall in a restricted range from 972 to 989 °C. Recall that low β_{rel} values are consistent with low a_{Al2O3}^{melt} and high a_{SiO2}^{melt} (Fig. 12; also see Eq. (11)). These grains may have formed in granites or felsites which have high silica activities, and typically have low estimated Al_2O_3 contents (e.g., Jolliff, 1991). Granites or felsites are not especially abundant in the Apollo collection, like the occurrence of the small number of β_{rel} values <0. It is also possible that these zircons might be products of quartz monzodiorite (QMD)-like liquids, which are also rare in the Apollo collection. The QMD clasts are most commonly found in Apollo sample 15405 (e.g., Meyer et al., 1996), though they are also present as soil particles in Apollo 14161 (Jolliff, 1991). If QMD-like rocks (or other high silica rocks) are due to fractional crystallization of KREEP basalts, as suggested by some (e.g., Ryder and Martinez, 1991; Jolliff, 1991; Snyder et al., 1995), then $\beta_{rel} < 0$ zircons may be related to zircons with β_{rel} = ~0.4.

The β_{rel} values indicate heterogeneities for pre-4.2 Ga grains, in agreement with heterogeneities from trace elements U and Th (e.g., Fig. 5a and b). We observe no clear correlation between X_{Al}^{Zrc} or β_{rel} and X_{Th}^{Zrc} or X_{U}^{Zrc} (EA-1). A correlation might be anticipated between the X_{Al}^{Zrc} or β_{rel} and the zircon Eu anomaly, however this is not observed. This is not necessarily surprising given the overall trace element variability among lunar rocks, even among different types of FHT rocks (e.g., Jolliff et al., 2000) or anorthosite clasts (e.g., Snyder et al., 1995; Pernet-Fisher et al., 2019), presumably reflecting variable assimilation of different rocks types. Note that the heterogeneities of trace elements and major rock-forming elements do not necessarily need to be coupled in the melt environment. Nevertheless, a consistent, broad conclusion emerges: zircon-saturated pre-4.2 Ga melts were heterogenous in trace elements and in $a_{Al2O3}^{melt} \pm a_{SiO2}^{melt}$. At the very least, processes that produced these zircons were diverse.

5.5.2. The origins of 4–4.2 Ga zircons based on β_{rel}

Most zircons in this age group cluster around β_{rel} values of about 1.1, suggesting that they can be considered as a suite of related samples. Possibilities for these zircon origins also include assimilation of anorthosite material or other Al_2O_3-rich phase assemblages (i.e., the Mg-suite rocks). That said, high temperature endogenous melts that can assimilate anorthosite material become harder to produce as the Moon cools. To our knowledge, the youngest Mg-suite rock (Apollo sample 67667) is ~4.2 Ga (Borg et al.

2015). Thus, there is a good probability that the Al_2O_3- rich rocks (inferred from the high β_{rel} zircon values) were the result of exogeneous impact-related events for zircons in this age range. There is also evidence for melts similar to the lower Al_2O_3 melts discussed for the pre-4.2 Ga grains, but the small number of samples does not allow a more detailed discussion at this point.

5.5.3. The origins of <4 Ga zircons based on β_{rel}

And finally, using the pre-4.0 Ga grains as a point of reference for processes that came first, we examine <4 Ga grains. The pronounced β_{rel} peak at ~0.7 for almost all <4 Ga grains is evidence for a common origin. We interpret this large homogeneous group of β_{rel} to be the result of one or more basin-forming impact events after 4 Ga. If these zircons did form within an impact melt sheet – possibly Imbrium – this begs the question regarding which rocks were melted. In the context of main melt compositions noted for the pre-4.2 suite, we hypothesize that parent melts for the ~3.94 Ga grains were formed from a mixture of the two main rock types identified in the pre-4.2 Ga samples. A ~3.94 Ga impact melt representing a mixture of these two rocks types is consistent with the upper ~15 km of the lunar crust being thoroughly mixed and melted. This also makes it unlikely that a monolithic primordial lunar rock was directly re-melted to produce the younger ~3.94 Ga zircons. In almost all cases, they must have been mixed with other sources to produce the observed of β_{rel} values.

6. CONCLUSIONS AND OUTLOOK

The pre-Nectarian lunar crust is the result of extreme differentiation, though available materials from this time period provide only fragmental coverage. Primary igneous rocks were broken, mixed, and re-melted >3.9 Ga, creating debris with complex and diverse histories. We sought to explore whether the chemistry of zircon can be used to help constrain magma compositions long lost. Our zircon U-Pb geochronology, coupled with detailed chemical characterization, show that individual zircon grains are indeed a useful resource to explore the pre-3.9 Ga lunar crust.

Mafic melts must fractionate to a more felsic residual before zircon saturation is realized; to provide information bearing on the point of melt evolution that our out-of-context zircons record, we measured Ti contents to constrain crystallization temperatures. We propose a revised titania activity model for lunar melts, based on the presence of ilmenite, Fe-metal, and constrained oxygen fugacity. The silica activity was also reasonably constrained for zircons orphaned from their source rocks. Overall, the a_{TiO2} and a_{SiO2} are expected to have sub-unity values that are broadly comparable; we predict that the range of values for a_{TiO2} is from 0.45 to 0.65, and that a_{SiO2} ranges from >0.45 to 1. We used this information to calculate the crystallization temperatures, with estimated uncertainties of ~70°, which was then used to anchor other investigations of zircon chemistry.

Our investigations of REE patterns show no systematic changes with age or, for the most part, with temperature. The exceptions are two Apollo 14311 and 14259 zircon fragments with calculated crystallization temperatures <800 °C, also with prominent Ce anomalies of 7 and 14. This study marks the first-time lunar zircons with Ce anomalies of this magnitude that have been documented outside of Apollo sample 14321. While we cannot rule out a terrestrial origin for grains of this nature, we consider it more probable that the zircons crystallized on the Moon in a highly fractionated volatile-present system.

There does not seem to be a strong, predictable correlation between ΣREE + Y and P content. Zircon REEs are most likely indicative of small-scale trace element variability in residual melts crystallizing zircon, conflated with charge coupling of REE and P, and possibly disequilibrium partitioning. Thus, zircon REE patterns are generally not the best sources of information about differences in the crystallization environment, at least for the zircons studied here.

Trace elements U and Th in zircon did yield some information bearing upon secular changes in melt heterogeneity. In particular, the spread in Th and U concentrations – calculated from initial values to account for radioactive decay of Th and U – show that pre-4.2 Ga systems were heterogenous when compared to post-4.2 Ga zircon bearing systems. The implications of the former are important because it provides strong evidence that the distributions of heat-producing elements in the pre-4.2 Ga lunar crust were heterogenous.

We also show that incorporation of trace amounts of the (generally overlooked) major rock-forming elements into the zircon structure can yield unique insights into the composition of zircon parent melts. We predict that X_{Fe}^{Zrc} should be sensitive to T and oxygen fugacity, and our analysis suggests some sensitivity to both. Further work will be required to take advantage of X_{Fe}^{Zrc} as a tool to explore source melt characteristics, such as zircon-melt Fe partitioning studies under fO_2- and a_{FeO}-buffered conditions. Perhaps the most informative data collected come from X_{Al}^{zrc} measurements. When combined with a thermodynamic model, results point to diverse melt compositions for the pre-4.2 Ga zircons investigated here. More than that, most pre-4.2 Ga grains show evidence for genesis in magmas characteristic of two dominant rock types. We interpret high β_{rel} zircons to have formed as a product of the interaction of hot Mg-rich mantle-derived melts with urKREEP and ferroan anorthosites, though crystallization from an alumina-rich impact-generated melt remains a viable possibility. We interpret the β_{rel} values centered around 0.4 as resulting from melting of the urKREEP source. Evidence for one other small group of pre-4.2 Ga zircon melt composition was detected. These contain very low X_{Al}^{Zrc} when compared to other zircons with similar crystallization temperatures. Our thermodynamic treatment shows that zircons with this characteristic are consistent with high a_{SiO2} (possibly quartz-saturated systems) and low a_{Al2O3}. Such zircons may be derived from quartz monzodiorites, like 15405 (e.g., Meyer et al., 1996), which may be products of fractionated KREEP basalts. These rock clasts also contain ilmenite, Fe-metal and SiO_2, (e.g., Ryder, 1976; Taylor et al., 1980) which represent important buffering phases in the reactions presented here and may thus represent a key

source of comparison in future studies. Other possibilities include granites or felsites, which also have high silica activities. The diverse pre-4.2 Ga melt compositions – reinforced by robust age constraints possible by U-Pb zircon geochronology – support the view that the early Moon was not a simple, globally stratified structure.

Evidence for the homogenization of different rock types also shows up in the chemical characteristics of younger zircons. The two major compositions detected in pre-4.2 Ga zircons broadly straddle the compositional characteristics of most <4.0 Ga grains, indicating that older primordial rocks could have been mixed and re-melted to form the vast majority of the <4.0 Ga grains. Our approach to better define origins of detrital lunar zircons will become more definitive with further zircon crystallization experiments using melt compositions appropriate to the early lunar environment.

Declaration of Competing Interest

The authors declare that they have no known competing financial interests or personal relationships that could have appeared to influence the work reported in this paper.

ACKNOWLEDGEMENTS

We thank James Day, two anonymous reviewers, and the Associate Editor Audrey Bouvier for comments that improved the presentation and quality of this contribution. We thank NASA and CAPTEM who made the samples available for study. This work was partially supported by NSF grant EAR-1650033, NASA PCE3 grant 80NSSC19M0069, and by the NASA Solar System Workings grant 80NSSC20K1039. The ion microprobe facility at UCLA is partially supported by the Instrumentation and Facilities Program, Division of Earth Sciences, NSF (EAR-1734856). Ming-Chang Liu is thanked for technical assistance on the UCLA ims1290 ion microprobe. We thank Carolyn Crow for her assistance during sample crushing, zircon separation and grain picking, and Elizabeth Bell for her assistance with REE + P + Mg + Fe measurements with the UCLA ims1270 ion microprobe. We thank Mike Ackerson, Carolyn Crow, Haolan Tang, Miki Nakajima, Paul Warren, and Yanling Wang for many interesting discussions.

APPENDIX A. SUPPLEMENTARY MATERIAL

Supplementary data to this article can be found online at https://doi.org/10.1016/j.gca.2020.06.018.

REFERENCES

Abramov O. and Mojzsis S. J. (2009) Microbial habitability of the Hadean Earth during the late heavy bombardment. *Nature* **459**, 419–422.

Aitken F. K., Anderson D. H., Bass M. N., Brown R. W., Butler, , P., Heiken G., Jakeg P., Reid A. M., Ridley W. I., Takeda H., Warner J. and Williams R. J. (1971) Apollo 14: Nature and origin of rock types in soil from the Fra Mauro formation. *Earth Planet. Sci. Lett.* **12**, 49–54.

Barboni M., Boehnke P., Keller C. B., Kohl I. E., Schoene B., Young E. D. and McKeegan K. D. (2017) Early formation of the Moon 4.51 billion years ago. *Sci. Adv.* **3**, e1602365.

Bell E. A., Boehnke P. and Harrison T. (2016) Recovering the primary geochemistry of Jack Hills zircons through quantitative estimates of chemical alteration. *Geochim. Cosmochim. Acta* **191**, 187–202.

Bell E. A., Boehnke P., Hopkins-Wielicki M. D. and Harrison T. M. (2015) Distinguishing primary and secondary inclusion assemblages in Jack Hills zircons. *Lithos* **234–235**, 15–26.

Bellucci J. J., Nemchin A. A., Grange M., Robinson K. L., Collins G., Whitehouse M. J., Snape J. F., Norman M. D. and Kring D. A. (2019) Terrestrial-like zircon in a clast from an Apollo 14 breccia. *Earth Planet. Sci. Lett.* **510**, 173–185.

Boehnke P. and Harrison T. M. (2016) Illusory Late Heavy Bombardments. *Proc. Natl. Acad. Sci.* **113**, 10802–10806.

Boehnke P., Watson E. B., Trail D., Harrison T. M. and Schmitt A. K. (2013) Zircon saturation re-revisited. *Chem. Geol.* **351**, 324–334.

Borg L. E., Gaffney A. M. and Shearer C. K. (2015) A review of lunar chronology revealing a preponderance of 4.34-4.37 Ga ages. *Meteorit. Planet. Sci.* **50**, 715–732.

Brasser R., Mojzsis S. J., Werner S. C., Matsumura S. and Ida S. (2016) Late veneer and late accretion to the terrestrial planets. *Earth Planet. Sci. Lett.* **455**, 85–93.

Chyba C. F., Thomas P. J., Brookshaw L. and Sagan C. (1990) Cometary delivery of organic molecules to the early earth. *Science* **249**, 366–373.

Cohen B. A., Swindle T. D. and Kring D. A. (2000) Support for the lunar cataclysm hypothesis from lunar meteorite impact melt ages. *Science* **290**, 1754–1756.

Crow C. A., McKeegan K. D. and Moser D. E. (2017) Coordinated U-Pb geochronology, trace element, Ti-in-zircon thermometry and microstructural analysis of Apollo zircons. *Geochim. Cosmochim. Acta* **202**, 264–284.

Cherniak D. J. and Watson E. B. (2000) Pb diffusion in zircon. *Chemical Geology*, 5–24.

Dickinson J. E. and Hess P. C. (1982) Zircon saturation in lunar basalts and granites. *Earth Planet. Sci. Lett.* **57**, 336–344.

Dygert N., Lin J. F., Marshall E. W., Kono Y. and Gardner J. E. (2017) A low viscosity lunar magma ocean forms a stratified anorthitic flotation crust with mafic poor and rich units. *Geophys. Res. Lett.* **44**, 11282–211291.

El Goresy A., Ramdohr P. and Taylor L. A. (1971) The geochemistry of opaque minerals in Apollo 14 crystalline rocks. *Earth Planet. Sci. Lett.* **13**, 121–129.

Elardo S. M., Draper D. S. and Shearer C. K. (2011) Lunar Magma Ocean crystallization revisited: Bulk composition, early cumulate mineralogy, and the source regions of the highlands Mg-suite. *Geochim. Cosmochim. Acta* **75**, 3024–3045.

Ferry J. M. and Watson E. B. (2007) New thermodynamic models and revised calibrations for the Ti-in-zircon and Zr-in-rutile thermometers. *Contrib. Miner. Petrol.* **154**, 429–437.

Gancarz A. J., Albee A. L. and Chodos A. A. (1971) Petrologic and Mineralogic investigation of some crystalline rocks returned by the Apollo 14 mission. *Earth Planet. Sci. Lett.* **12**, 1–18.

Genda H., Brasser R. and Mojzsis S. J. (2017) The terrestrial late veneer from core disruption of a lunar-sized impactor. *Earth Planet. Sci. Lett.* **480**, 25–32.

Ghiorso M. S. and Gualda G. A. R. (2013) A method for estimating the activity of titania in magmatic liquids from the compositions of coexisting rhombohedral and cubic iron–titanium oxides. *Contrib. Miner. Petrol.* **165**, 73–81.

Gomes R., Levison H. F., Tsiganis K. and Morbidelli A. (2005) Origin of the cataclysmic Late Heavy Bombardment period of the terrestrial planets. *Nature* **435**, 466–469.

Grange M. L., Nemchin A. A. and Pidgeon R. T. (2013a) The effect of 1.9 and 1.4 Ga impact events on 4.3 Ga zircon and

phosphate from an Apollo 15 melt breccia. *J. Geophys. Res. Planets* **118**, 2180–2197.

Grange M. L., Nemchin A. A., Pidgeon R. T., Timms N., Muhling J. R. and Kennedy A. K. (2009) Thermal history recorded by the Apollo 17 impact melt breccia 73217. *Geochim. Cosmochim. Acta* **73**, 3093–3107.

Grange M. L., Nemchin A. A., Timms N., Pidgeon R. T. and Meyer C. (2011) Complex magmatic and impact history prior to 4.1Ga recorded in zircon from Apollo 17 South Massif aphanitic breccia 73235. *Geochim. Cosmochim. Acta* **75**, 2213–2232.

Grange M. L., Pidgeon R. T., Nemchin A. A., Timms N. E. and Meyer C. (2013b) Interpreting U-Pb data from primary and secondary features in lunar zircon. *Geochim. Cosmochim. Acta* **101**, 112–132.

Gross J. and Treiman A. H. (2011) Unique spinel-rich lithology in lunar meteorite ALHA 81005: Origin and possible connection to M3 observations of the farside highlands. *J. Geophys. Res.* **116**. https://doi.org/10.1029/2011JE003858.

Grange M. L., Pidgeon R. T., Nemchin A. A., Timms N. E. and Meyer C. (2013) Interpreting U-Pb data from primary and secondary features in lunar zircon. *Geochimica et Cosmochimica Acta* **101**, 112–132.

Haggerty S. E. (1973) Luna 20: mineral chemistry of spinel, pleonaste, chromite, ulvospinel, ilmenite and rutile. *Geochim. Cosmochim. Acta* **37**, 857–867.

Haggerty S. E. and Meyer H. O. A. (1970) Apollo 12: opaque oxides. *Earth Planet. Sci. Lett.* **9**, 379–387.

Hartmann W. K. (1975) Lunar "Cataclysm": a misconception? *Icarus* **24**, 181–187.

Hauri E. H., Weinreich T., Saal A. E., Rutherford M. C. and Van Orman J. A. (2011) High pre-eruptive water contents preserved in lunar melt inclusions. *Science* **333**, 213–215.

Hayden L. A. and Watson E. B. (2007) Rutile saturation in hydrous siliceous melts and its bearing on Ti- thermometry of quartz and zircon. *Earth Planet. Sci. Lett.* **258**, 561–568.

Hinton R. W. and Meyer C. (1991) Ion probe analyses of zircon and yttrobetafite in a lunar granite. *LPSC* **XXII**, 575–576.

Hirschmann M. M., Withers A. C., Ardia P. and Foley N. T. (2012) Solubility of molecular hydrogen in silicate melts and consequences for volatile evolution of terrestrial planets. *Earth Planet. Sci. Lett.* **345–348**, 38–48.

Hlava P. F., Prinz M. and Keil K. (1972) Niobian rutile in an Apollo 14 KREEP fragment. *Meteoritics* **7**, 479–486.

Hopkins M. and Mojzsis S. J. (2015) A protracted timeline for lunar bombardment from mineral chemistry, Ti thermometry and U-Pb geochronology of Apollo 14 melt breccia zircons. *Contr. Mineral. Petrol.* **169**. https://doi.org/10.1007/s00410-00015-01123-x.

Jolliff B. L. (1991) Fragments of quartz monzodiorite and felsite in apollo 14 soil particles. *Proc Lunar and Planetary Sci Conf.* **21**, 101–118.

Jolliff B. L., Gillis J. J., Haskin L. A., Korotev R. L. and Wieczorek M. A. (2000) Major lunar crustal terranes: Surface expressions and crust-mantle origins. *J. Geophys. Res.* **105**, 4197–4216.

Karner J. M., Sutton S. R., Papike J. J., Schearer C. K., Jones J. H. and Newville M. (2006) Application of a new vanadium valence oxybarometer to basaltic glasses from the Earth, Moon, and Mars. *American Mineralogist* **91**, 270–277.

Labotka T. C., Kempa M. J., White C., Papike J. J. and Laul J. C. (1980) The lunar regolith – Comparative petrology of the Apollo sites. In *Proc. Lunar and Planetary Science Conference*, 11, pp. 1285–1305. Proc. Lunar and Planetary Science Conference.

Laneuville M., Wieczorek M. A., Breuer D. and Tosi N. (2013) Asymmetric thermal evolution of the Moon. *J. Geophys. Res. Planets* **118**, 1435–1452.

Laneuville M., Taylor J. and Wieczorek M. A. (2018) Distribution of radioactive heat sources and thermal history of the Moon. *J. Geophys. Res. Planets* **123**, 3144–3166.

Liu M. C., McKeegan K. D., Harrison T. M., Jarzebinski G. and Vlava L. (2018) The Hyperion-II radio-frequency oxygen ion source on the UCLA ims1290 ion microprobe: Beam characterization and applications in geochemistry and cosmochemistry. *Int. J. Mass Spectrom.* **424**, 1–9.

Merle R. E., Nemchin A. A., Grange M. L., Whitehouse M. J. and Pidgeon R. T. (2014) High resolution U-Pb ages of Ca-phosphates in Apollo 14 breccias: Implications for the age of the Imbrium impact. *Meteorit. Planet. Sci.* **49**, 2241–2251.

Merle R. E., Nemchin A. A., Whitehouse M. J., Pidgeon R. T., Grange M. L., Snape J. F. and Thiessen F. (2017) Origin and transportation history of lunar breccia 14311. *Meteorit. Planet. Sci.* **52**, 842–858.

Meyer C., Williams I. S. and Compston W. (1996) Uranium-lead ages for lunar zircons: Evidence for a prolonged period of granophyre formation from 4.32 to 3.88 Ga. *Meteorit. Planet. Sci.* **31**, 370–387.

Mojzsis S. J. and Harrison T. M. (2002) Establishment of a 3.83-Ga magmatic age for the Akilia tonalite (southern West Greenland). *Earth Planet. Sci. Lett.* **202**, 563–576.

Morbidelli A., Lunine J. I., O'Brien D. P., Raymond S. N. and Walsh K. J. (2012) Building terrestrial planets. *Annu. Rev. Earth Planet. Sci.* **40**, 251–275.

Meyer C., Williams, I.S., and Compston, W. (1989) Zircon-containing rock fragments within Apollo 14 breccia indicate serial magmatism from 4350 to 4000 million years. In Workshop on Moon in Transition: Apollo 14 KREEP, and Evolved Lunar Rocks (eds. Taylor and Warren), pp. 75–78. LPI Tech. Rpt. 89–03.

Nash W. P. and Hausel W. D. (1973) Partial pressures of oxygen, phorphorus and fluorine in some lunar lavas. *Earth Planet. Sci. Lett.* **20**, 13–27.

Nemchin A. A., Grange M. L. and Pidgeon R. T. (2010) Distribution of rare earth elements in lunar zircon. *Am. Mineral.* **95**, 273–283.

Nemchin A. A., Grange M. L., Pidgeon R. T. and Meyer C. (2012) Lunar zirconology. *Aust. J. Earth Sci.* **59**, 277–290.

Nemchin A. A., Pidgeon R. T., Whitehouse M. J., Vaughan J. P. and Meyer C. (2008) SIMS U-Pb study of zircon from Apollo 14 and 17 breccias: Implications for the evolution of lunar KREEP. *Geochim. Cosmochim. Acta* **72**, 668–689.

Nemchin A. A., Whitehouse M. J., Pidgeon R. T. and Meyer C. (2006) Oxygen isotopic signature of 4.4–3.9Ga zircons as a monitor of differentiation processes on the Moon. *Geochim. Cosmochim. Acta* **70**, 1864–1872.

O'Neill H. S. C. (1987) Quartz-fayalite-iron and quartz-fayalite-magnetite equilibria and the free energy of formation of fayalite (Fe2SiO4) and magnetite (Fe3O4). *Am. Mineral.* **72**, 67–75.

O'Neill H. S. C., Pownceby M. I. and Wall V. J. (1988) Ilmenite-rutile-iron and ulvospinel-ilmenite-iron equilibria and the thermochemistry of ilmenite (FeTiO3) and ulvospinel (Fe2TiO4). *Geochim. Cosmochim. Acta* **52**, 2065–2072.

Papanastassiou D. A. and Wasserburg G. J. (1971) Rb-Sr ages of igneous rocks from the Apollo 14 mission and the age of the Fra Mauro. *Earth Planet. Sci. Lett.* **12**, 36–48.

Papike J. J., Simon S. B. and Laul J. C. (1982) The lunar regolith: chemistry, mineralogy, and petrology. *Rev. Geophys. Space Phys.* **20**, 761–826.

Papike J. J., Karner J. M. and Shearer C. K. (2016) Comparative planetary mineralogy: V/(Cr + Al) systematics in chromite as an indicator of relative oxygen fugacity. *Am. Mineral.* **89**, 1557–1560.

Pernet-Fisher J. P., Deloule E. and Joy K. H. (2019) Evidence of chemical heterogeneity within lunar anorthosite parental magmas. *Geochim. Cosmochim. Acta* **266**, 109–130.

Petro N. E. and Pieters C. M. (2008) The lunar-wide effects of basin ejecta distribution on the early megaregolith. *Meteorit. Planet. Sci.* **43**, 1517–1529.

Pidgeon R. T., Nemchin A. A., van Bronswijk W., Geisler T., Meyer C., Compston W. and Williams I. S. (2007) Complex history of a zircon aggregate from lunar breccia 73235. *Geochim. Cosmochim. Acta* **71**, 1370–1381.

Paces J. B. and Miller J. D. (1993) Precise U-Pb ages of Duluth Complex and related mafic intrusions, northeastern Minnesota: Geochronological insights to physical, petrogenetic, paleomagnetic, and tectonomagmatic processes associated with the 1.1 Ga Midcontinent Rift System. *Journal of Geophysical Research: Solid Earth* **98**, 13997–14013.

Quidelleur X., Grove M., Lovera O. M., Harrison T. M., Yin A. and Ryerson F. J. (1997) Thermal evolution and slip history of the Renbu Zedong Thrust, southeastern Tibet. *J. Geophys. Res. Solid Earth* **102**, 2659–2679.

Robie R. A. and Hemingway B. S. (1995) Thermodynamic properties of minerals and related substances at 298.15 K and 1 bar (10^5 Pascals) pressure and at higher temperatures. *U.S. Geol. Surv. Bull.* **2131**, 461 pp.

Ryder G. (1976) Lunar sample 15405: Remnant of a KREEP basalt-granite differentiated pluton. *Earth Planet. Sci. Lett.* **29**, 255–268.

Ryder G. and Bower J. F. (1976) Poikilitic KREEP impact melts in the Apollo 14 white rocks. *Proc Lunar Sci Conf.* **7**, 1925–1948.

Ryder G., Koeberl C. and Mojzsis S. J. (2000) Heavy Bombardment of the Earth at ∼3.85 Ga: the search for petrographic and geochemical evidence. *Origin of the Earth and Moon* **1**, 475–492.

Ryder G. and Martinez R. R. (1991) Evolved hypabyssal rocks from Station 7, Apennine Front, Apollo 15. In *Proceedings, 21st Lunar and Planetary Science Conference*, pp. 137–150.

Ryerson F. J. and Watson E. B. (1987) Rutile saturation in magmas: implications for Ti-Nb-Ta depletion in island-arc basalts. *Earth Planet. Sci. Lett.* **86**, 225–239.

Sañudo-Wilhelmy S. A. and Flegal A. R. (1994) Temporal variations in lead concentrations and isotopic composition in the Southern California Bight. *Geochim. Cosmochim. Acta* **58**, 3315–3320.

Sato M., Hickling N. L. and McLane J. E. (1973) Oxygen fugacity values of Apollo 12 14 and 15 lunar samples and reduced state of lunar magmas. In *Proceedings of the Fourth Lunar Science Conference, Supplement 4, Geochimica et Cosmochimica Acta*, 1, pp. 1061–1079. Proceedings of the Fourth Lunar Science Conference, Supplement 4, Geochimica et Cosmochimica Acta.

Schmitt A. K. and Vazquez J. A. (2006) Alteration and remelting of nascent oceanic crust during continental rupture: Evidence from zircon geochemistry of rhyolites and xenoliths from the Salton Trough, California. *Earth Planet. Sci. Lett.* **252**, 260–274.

Shearer C. K. et al. (2006a) Thermal and magmatic evolution of the Moon. *Rev. Mineral. Geochem.* **60**, 365–518.

Shearer C. K., Papike J. J. and Karner J. M. (2006b) Pyroxene europium valence oxybarometer: Effects of pyroxene composition, melt composition, and crystallization kinetics. *Am. Mineral.* **91**, 1565–1573.

Simonds C. H., Phinney W. C., Warner J. L., McGee P. E., Geeslin J., Brown R. W. and Rhodes J. M. (1977) Apollo 14 revisited, or breccias aren't so bad after all. In *Proc Lunar Science Conference 8th*, pp. 1869–1893.

Snape J. F., Nemchin A. A., Bellucci J. J., Whitehouse M. J., Tartèse R., Barnes J. J., Anand M., Crawford I. A. and Joy K. H. (2016a) Lunar basalt chronology, mantle differentiation and implications for determining the age of the Moon. *Earth Planet. Sci. Lett.* **451**, 149–158.

Snape J. F., Nemchin A. A., Grange M. L., Bellucci J. J., Thiessen F. and Whitehouse M. J. (2016b) Phosphate ages in Apollo 14 breccias: Resolving multiple impact events with high precision U-Pb SIMS analyses. *Geochim. Cosmochim. Acta* **174**, 13–29.

Snyder G. A., Taylor L. A. and Halliday A. N. (1995) Chronology and petrogenesis of the lunar highlands alkali suite: Cumulates from KREEP basalt crystallization. *Geochim. Cosmochim. Acta* **59**, 1185–1203.

Stadermann F. J., Heusser E., Jesseberger E. K., Lingner S. and Stöffler D. (1991) The case for a younger Imbrium basin: New 40Ar-39Ar ages of Apollo 14 rocks. *Geochim. Cosmochim. Acta* **55**, 2339–2349.

Stoffler D. (2006) Cratering history and lunar chronology. *Rev. Mineral. Geochem.* **60**, 519–596.

Strom R. G., Malhortra R., Ito T., Yoshida F. and Kring D. A. (2005) The origin of planetary impactors in the inner solar system. *Science* **309**, 1847–1850.

Sun Y., Li L. and Zhang Y. (2017) Detection of Mg-spinel bearing central peaks using M3 images: Implications for the petrogenesis of Mg-spinel. *Earth Planet. Sci. Lett.* **465**, 48–58.

Szymanowskia D., Fehr M. A., Guillong M., Coble M. A., Wotzlawa F., Nasdala L., Ellis B. S., Bachmann O. and Schönbächler M. (2018) Isotope-dilution anchoring of zircon reference materials for accurate Ti-in-zircon thermometry. *Chem. Geol.* **481**, 146–154.

Taylor D. J., McKeegan K. D. and Harrison T. M. (2009) Lu–Hf zircon evidence for rapid lunar differentiation. *Earth Planet. Sci. Lett.* **279**, 157–164.

Taylor L. A., McCallister R. H. and Sardi O. (1973) Cooling histories of lunar rocks based on opaque mineral geothermometers. In *Proceedings of the 4th Lunar Science Conference*, 1, pp. 819–828. Proceedings of the 4th Lunar Science Conference.

Taylor L. A., Williams R. J. and McCallister R. H. (1972) Stability relations of ilmenite and ulvöspinel in the Fe-Ti-O system and application of these data to lunar mineral assemblages. *Earth Planet. Sci. Lett.* **16**, 282–288.

Taylor L. A., Shervais J. W., Hunter R. H., Shih C.-Y., Wooden J., Nyquist L. E. and Laul L. C. (1983) Pre-4.2 AE mare-basalt volcanism in the lunar highlands. *Earth Planet. Sci. Lett.* **66**, 33–47.

Tera F., Papanastassiou D. A. and Wasserburg G. J. (1974) Isotopic evidence for a terminal lunar cataclysm. *Earth Planet. Sci. Lett.* **22**, 1–21.

Thomas J. B., Watson E. B., Spear F. S., Shemella P. T., Nayak S. K. and Lanzirotti A. (2010) TitaniQ under pressure: the effect of pressure and temperature on the solubility of Ti in quartz. *Contrib. Miner. Petrol.* **160**, 743–759.

Tompkins S. and Pieters C. M. (1999) Mineralogy of the lunar crust: results from clementine. *Meteorit. Planet. Sci.* **34**, 25–41.

Treiman A. H., Kulis M. J. and Glazner A. F. (2019) Spinel-anorthosites on the Moon: Impact melt origins suggested by enthalpy constraints. *Am. Mineral.* **104**, 370–384.

Trail D., Tailby N. D., Wang Y., Harrison T. M. and Boehnke P. (2017) Aluminum in zircon as evidence for peraluminous and metaluminous melts from the Hadean to present. *Geochem. Geophys. Geosyst.*. https://doi.org/10.1002/2016GC006794 1-14.

Trail D., Thomas J. B. and Watson E. B. (2011a) The incorporation of hydroxyl into zircon. *Am. Mineral.* **96**, 60–67.

Trail D., Watson E. B. and Tailby N. D. (2011b) The oxidation state of Hadean magmas and implications for early Earth's atmosphere. *Nature* **480**, 79–82.

Trail D., Watson E. B. and Tailby N. D. (2012) Ce and Eu anomalies in zircon as proxies for the oxidation state of magmas. *Geochimica et Cosmochimica Acta* **97**, 70–87.

Taylor G. J., Warner R. D. and Keil K. (1980) Silicate liquid immiscibility, evolved lunar rocks and the formation of KREEP. *Proc Conf. Lunar Highlands Crust*, p339–352.

Urey H. C. (1966) Chemical evidence relative to the solar system. *Mon. Not. R. Astr. Soc.* **131**, 199–223.

Wadhwa M. (2008) Redox conditions on small bodies, the moon and mars. *Rev. Mineral. Geochem.* **68**, 493–510.

Wang Y. and Trail D. (2019) Aluminium partitioning between zircon and haplogranitic melts: the influence of temperature and melt composition. *Chem. Geol.* **501**, 71–80.

Warren P. (1985) The magma ocean concept and lunar evolution. *Ann. Rev. Earth Planet. Sci.* **13**, 201–240.

Warren P. and Wasson J. T. (1979) The origin of KREEP. *Rev. Geophys. Space Phys.* **17**, 73–88.

Warren P. H., Taylor G. J., Keil K., Kallemeyn G. W., Rosener P. S. and Wasson J. T. (1983) Sixth foray for pristine nonmare rocks and an assessment of the diversity of lunar anorthosites. In *Proc. Lunar Planet. Sci. Conf. 13, in J. Geophys. Res.*, pp. A615–A630.

Watson E. and Harrison T. (2005) Zircon thermometer reveals minimum melting conditions on earliest Earth. *Science* **308**, 841–844.

Wieczorek M. A. et al. (2006) The constitution and structure of the lunar interior. *Rev. Mineral. Geochem.* **60**, 221–364.

Wiedenbeck M. et al. (2004) Further characterisation of the 91500 zircon crystal. *Geostand. Geoanal. Res.* **28**, 9–39.

Wielicki M. M., Harrison T. M. and Schmitt A. K. (2012) Geochemical signatures and magmatic stability of terrestrial impact produced zircon. *Earth Planet. Sci. Lett.* **321–322**, 20–31.

White L. F., Černok A., Darling J. R., Whitehouse M. J., Joy K. H., Cayron C., Dunlop J., Tait K. T. and Anand M. (2020) Evidence of extensive lunar crust formation in impact melt sheets 4330 Myr ago. *Nat. Astron.*. https://doi.org/10.1038/s41550-41020-41092-41555.

Wood J. A., Dickey J. S., Marvin U. B. and Powell B. N. (1970) Lunar anorthosites and a geophysical model of the moon. In *Proceedings of the Apollo Lunar Science Conference*, 1, pp. 965–988. Proceedings of the Apollo Lunar Science Conference.

Wopenka B., Jolliff B. L., Zinner E. and Kremser D. (1996) Trace element zoning and incipient metamictization in a lunar zircon: Application of three microprobe techniques. *Am. Mineral.* **81**, 902–912.

Zellner N. E. B. (2017) Cataclysm no more: new views on the timing and delivery of lunar impactors. *Orig. Life Evol. Biosph.* **47**, 261–280.

Associate editor: Audrey Bouvier